Arab American University

Faculty of Graduate Studies

Optical dynamics at Se/$CdBr_2$ interfaces

By

Salsabeel Nedal Na'em Imair

Supervisor

Prof. Dr. Atef Qasrawi

This Thesis was submitted in partial fulfillment of the requirements for

the Master's degree in Physics

May/2022

Optical dynamics at Se/$CdBr_2$ interfaces

By

Salsabeel Nedal Naem Imair

This thesis was defended successfully on May 25th 2022 and approved by:

Committee members	Signature
1. Supervisor: Prof. Dr. Atef Fayez Qasrawi	.....
2. External examiner: Prof. Dr. Mohammad El-Said	.....
3. Internal Examiner: Prof. Dr. Hazem Khanfar	.....

Declaration

The work provided in this thesis, unless otherwise referenced, is the researcher's own work, and has not been submitted elsewhere for any other degree or qualification.

العمل المقدم في هذه الرسالة, ما لم تتم الاشارة الى غير ذلك, هو عمل الباحث الخاص ولم يتم تقديمه في أي مكان اخر للحصول على أي درجة أو مؤهل اخر.

Student's Name: Salsabeel Nedal Imair

Signature: سلسبيل عمير

Data: ١٠/١٧ ٢٠٢٢

Acknowledgments

In the name of God, the Most Gracious, the Most Merciful, and my success is only by Allah. My master's thesis has been completed from my prestigious university, Arab American University, thanks to God. I extend my sincere thanks and appreciation to all faculty members. In particular, the honorable Professor Dr. Atef Qasrawi, who has spared no effort in order for this thesis to see the light. God rewarded him with the best reward. And I also thanks to the external examiner, the virtuous Prof. Dr. Mohammad El-Said, and the internal examiner, the virtuous Prof. Dr. Hazem Khanfar.

Thanks are also due to the cutes and beautiful colleagues Rana ,lara, wala and bayan who provided me with support and assistance, both in the practical and theoretical side throughout the work.

All thanks and love to my beautiful family who supported me all the time. My dear parents, (my mother and my father) and my beautiful sister zainab , cute brothers ibrahem ,ismaeal ,ahmad and adam, whose prayers for me was the secret of my success. My hope and happiness are you.

Thank are also for my wonderful friends, Rawa', Suzan and Maisam, who were distinguished by loyalty and giving, and we walked together on the path to success. Praise be to God , and we will continue.

Abstract

Optical dynamics at Se/$CdBr_2$ interfaces

In the current work, we designed and characterized a new class of optical receivers. The optical interfaces are fabricated by the physical vapor deposition of $CdBr_2$ onto selenium substrates. The compositional, optical and dielectric properties of the Se/$CdBr_2$ films are investigated in details. It is observed that thin films of selenium exhibit structural transitions from amorphous to polycrystalline phases after four weeks of deposition. The formed hexagonal phase of selenium strongly interacted with the hexagonal $CdBr_2$ forming novel characteristics. From structure point of view, coating of $CdBr_2$ onto Se decreases the defect density of Se, increase the crystallite sizes and lowered the percentage of stacking faults. Optically, Urbech's band tails are formed, free carrier absorption is enhanced, the energy band gap of selenium shrinks. The formation of Se/$CdBr_2$ interfaces is accompanied by the conduction and valence band offsets 1.25 eV and 0.63 eV, respectively. On the other hand, the dielectric dispersion analyses have shown that the formation of Se/$CdBr_2$ results in resonant dielectric spectra. The real part of the dielectric spectra of Se, $CdBr_2$ and Se/$CdBr_2$ have shown the possible formation of two dielectric resonators centered in the visible and near infrared ranges of light. The study here additionally included the optimization of the optical conductivity parameters for Se/$CdBr_2$ optical receivers. It was observed that the interfaces exhibit more efficient drift mobility with a Plasmon frequency that suits 4G/5G communication technology. We believe that optical interfaces can perform well in the optical communication technology.

List of Content

List of Tables

List of Figures

List of Symbols

Symbol	Symbol Meaning
Se	Selenium
CdBr2	Cadmium bromide
Se/CdBr2	Selenium /Cadmium bromide
XRD	X-ray diffraction
Δ	The lattice mismatch
a	Lattice Constant
hkl	Miller indices
Eg	Energy band gap
k	Scherre's constant
θ	Bragg angle
d	Inter-planner distance
λ	Wavelength
n	Integer
A^o	Angstrom.
D	Crystallite Size
β	The peak broadening at full width half maximum peak in radians
SF	The staking factor
ε	Strain
δ	Dislocation density
α	Absorption Coefficient
E_e	The width of the band tails
ε_1 (E)	The real part of the dielectric constant
$\boldsymbol{\varepsilon}_{eff}$	The effective dielectric constant
T	Transmittance
R	Reflectance
X	The electron affinity

Chapter One

Introduction

Selenium (Se) is an important semiconductor and is one of the most widely studied elements due to its unique physical properties such as high photo-conductivity, low solubility, high thermoelectric reactivation [1], and high resistance to dark conditions [2]. Selenium is an essential element with physical, chemical and biochemical properties, that plays an important role in human health. For examples, it can provide anti-cancer and enhance human immunity as a catalytic center of enzymes [3]. Recent studies have shown the effect of selenium on COVID-19 patients through the production of antibodies and enhancement of the cell maturation and function laity [4]. Selenium nanoparticles have special interest because they have positive impact on planet organism function that can enhance antioxidant potential [3]. Selenium is used as a nano-sheet transistor in the manufacture of electrolyte gate devices, as it provides low energy consumption [5]. Experimentally amorphous selenium thin films mentioned to be an interesting material for use in the fabrication of many optical and optoelectric devices [6]. In addition, Se is used as a material in X-ray filament detector arrays, medical image sensors to improve the thermal stability of photo sensor and superconductors [7].

Moreover, the trigonal selenium as a semiconductor has a direct band gap of 1.95 eV. It is an absorber that provides the potential for the low cost fabrication of efficient solar cells [8]. For examples, $Cu_2ZnSn(S, Se)$ absorber are materials that are used in manufacturing single-junction solar cells or as a part of a tandem device structure in thin film photovoltaic devices [9].

On the other hand, cadmium bromide ($CdBr_2$) compounds have attracted the attention of researchers because they can be used in different application. One of these applications use a cadmium chalcogenides as a thin film of wide band gap semiconductor, suitable for fabricating quantum dots [10].

In addition, using $CdBr_2$ as vander waals, $CdBr_2$ micro/nanotubes were employed as photo detectors, showing high current responsively [11,12] . As there is always a need to produce and develop new classes of optoelectronic devices, that fit well with technology updates, here in this work, we target fabricating new classes of thin film heterojunction devices benefiting from Se and $CdBr_2$. These devices are to perform as multiple functional devices. Since we are interested in obtaining high performance thin film light absorbers. We chose selenium thin film as a good absorber and cadmium bromide is considered an optimistic a bilayer for the preparation of heterojunction.

Both the Se and $CdBr_2$ films are prepared by different deposition techniques. It's mentioned that $CdBr_2$, can be prepared by a thermal evaporation deposition technique under a low vacuum pressure [13]. Furthermore, compound thin films are composed of Se produced by chemical vapor deposition (CVD) and physical vapor deposition (PVD) techniques. In addition, Se sources are prepared by the pulsed laser deposition (PLP) technique [14]. Moreover, $CdS/CdBr_2$ hetero-nanojunction doped with Mn was prepared by one – step synthesis and manufacturing by the chemical vapor deposition method of high purity CdS[15].

Selenium is expected to play an important role in optoelectronic technology. In this work, we are motivated to produce new types of devices. Cadmium bromide is regarded as a promising substrate for the preparation of heterojunction that can be used in electric circuits and sensors.

In the current work, we will first focus on the preparation and on the film's basic physical characteristics. Then the nature of the formation of the films, in addition to the chemical stoichiometry, will be considered. From practical of view, we will focus on the optical properties of the films in an attempt to use them as optical absorbers. Particularly, the effect of $CdBr_2$ layer on the optical performance of Se will be considered. In addition, the enhancement in the dielectrically properties of the films will be taken into account. Moreover, computer simulation that imposes the Drude – Lorentz method to explore the optical conductivity parameters will also be considered. The thesis will report the drift mobility, the plasma frequency, the free hole density and the oscillator energies of the Se/$CdBr_2$ optical receives.

The thesis here will be composed of the theoretical parts as in chapter two. This chapter will report all the mathematical relations used to explain the results. The setup of the experiments employed to handle the characteristics of the films will be reported in chapter three. In addition, chapter four of this thesis will focus on the main results we obtained for the heterojunction devices. Some of the concluding remarks will be mentioned in chapter five.

Chapter Two

Theoretical Background

2.1 X-Ray Diffraction (XRD):

X−rays are short electromagnetic waves that appear in the electromagnetic spectrum between $0.1 - 100\ A^o$ [16]. In this work we are interested in the x−ray diffraction (XRD) technique. X−ray diffraction is the most effective method, which is rapid and powerful, in the analytical technological field used for characterization a solid−state materials and identifying their structural nature. It is based on the concepts of Bragg's law. Further details are given in the following subsections.

2.1.1 Bragg's Law:

Consider a crystal specimen that consists of parallel planes of atoms in a lattice, spaced a distance (d) an inter plane between atomic planes. When a monochromatic X−ray beam is incident onto specimen under study, with a known wavelength (λ). It's angle of incident (θ) will be reflected by the same scattering angle θ. Constructive interference occurs when the path different between two rays is equal integer multiple (n) of wavelength [15]. The case of a beam diffracted by an atomic plane is represented in fig. 2.1. Bragg's law states that [16]:

$$2d\ sin\theta = n\lambda \qquad (2.1)$$

Where θ a diffraction angle between incident ray and plane surface, d inter planner spacing which is $1.5405\ A^o$ and n the integer number reflecting the order of diffraction.

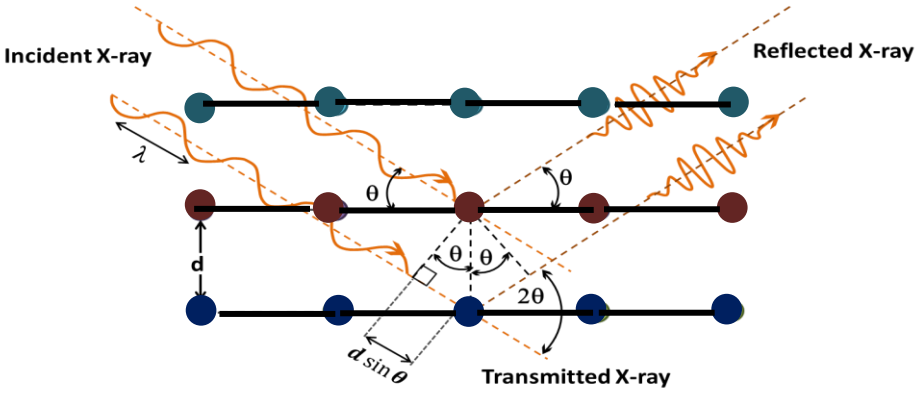

Fig. 2.1: The schematic diagram of Bragg's law.

Through using Bragg's equation, if the interplanar distance is known, it can be used to identify the crystal structure where a , b and c are lattice constants and hkl are the miller index for crystal planes as defined in the following table [17]:

Table 2.1: The spacing interplanar formula for the six structures.

crystal System	**Spacing Interplanar**
Cubic	$\frac{1}{d^2} = \frac{(h^2+k^2+l^2)}{a^2}$
Hexagonal	$\frac{1}{d^2} = \frac{4}{3a^2}(h^2+hk+k^2) + \frac{l^2}{c^2}$
Trigonal	$\frac{1}{d^2} = \frac{4}{3a^2}(h^2+hk+k^2) + \frac{l^2}{c^2}$
Tetragonal	$\frac{1}{d^2} = \frac{1}{a^2}(h^2+k^2) + \frac{l^2}{c^2}$
Orthorhombic	$\frac{1}{d^2} = \frac{h^2}{a^2} + \frac{k^2}{b^2} + \frac{l^2}{c^2}$
Monoclinic	$\frac{1}{d^2} = \frac{h^2}{a^2\sin^2\beta} + \frac{k^2}{b^2} + \frac{l^2}{c^2\sin^2\beta} - \frac{2hlcos\beta}{ac\sin^2\beta}$

2.1.2 Scherrer Equation and Structural Characterizations:

The diffraction effects on the structural properties of materials involve diffraction angles and intensities. Analysis of the diffraction patterns leads to information about the crystal size. The well-known Scherrer equation that is used to determine the crystallite size for the most intensive peak broadening [18] in the x−ray diffraction patterns is derived below. The Scherrer equation could be found in general form by the derivation of Bragg's law, multiplying each side of Bragg's equation 2.1 by an integer *c* with change *cd* by *t*, which *t* is the crystal thickness, assuming n=1 to get:

$$c\lambda = 2\, cd \sin\theta \qquad (2.2)$$

$$c\lambda = 2\, t \sin\theta \qquad (2.3)$$

Here, equation 2.3 becomes the c^{th} order reflection of a total plane with an inter planner distance t. From the derivative of both sides of equation 2.4:

$$0 = 2\Delta t \sin\theta + 2t \cos\theta\, \Delta\theta \qquad (2.4)$$

$$t = \frac{\Delta t\, .\sin\theta}{\cos\theta\ \ \Delta\theta} \qquad (2.5)$$

as well as $\Delta\theta$ possibilities, positive or negative. Thus, an absolute value must be used. Applying the $\Delta t = d$, $t = D$ and substituting $\frac{\lambda}{2}$ for $d \sin\theta$ from Bragg's law to becomes:

$$D = \frac{\lambda}{2\cos\theta.\Delta\theta} \qquad (2.6)$$

Where $\Delta\theta$ represents the half width of the peaks, in order that $2\Delta\theta$ is the full width of the peak at half maximum (β) from that substitution β for $2.\Delta\theta$, where is the angular width, D is the crystalline size equation as:

$$D = \frac{\lambda}{\beta \cos\theta} \tag{2.7}$$

In addition, for many cases, it shows the exact scherrers equation which is multiplied by k with λ:

$$D = \frac{k\lambda}{\beta \cos\theta} \tag{2.8}$$

Were k is the scherrer constant, it depends on the crystalline shape, λ is the wavelength of incident x−ray, β is the line broadening of half the maximum intensity determined in radians, and θ is the Bragg angle. Where β is the fall width at half maximum of diffraction peaks in radians (FWHM), D is the grain size of crystallite, $K = 0.94$ a geometric constant for a crystallite shape [19]. For more information about different structural properties produced by the peak broadening as exhibited in fig. 2.2.**[**20] shows the full peak intensity analysis. As such, the crystallite size (D) was defined as:

" the diameter of an individual crystallite in the crystal" [21].

The full width of half the maximum is measured by help of fig. 2.2:

$$D = \frac{B + C}{2} \tag{2.9}$$

$$E = \frac{A - D}{2} \tag{2.10}$$

The value of FWHM $= E + D$, which apply to form β [22]:

$$\beta = \tfrac{1}{2}\,(2\theta_{max} - 2\theta_{min}) \times \left(\tfrac{3.14}{180}\right) \tag{2.11}$$

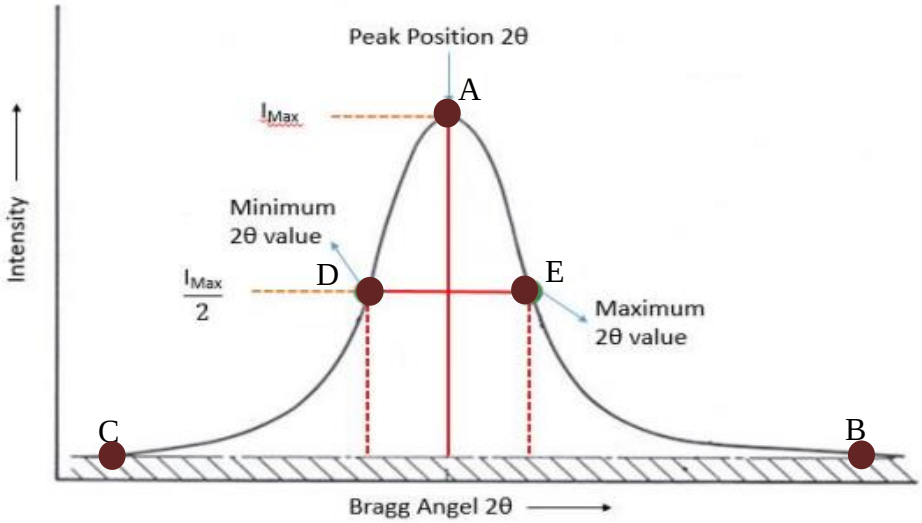

Fig. 2.2: the full width at half maximum (FWHM) .

Strain (ε): the ratio of contraction or expansion in broadening length to the original length [23], or can mean the variation on the individual crystallite lattice parameter in terms of root mean square:

$$\varepsilon = \frac{\beta}{4\tan(\theta)} \tag{2.13}$$

Dislocation density (δ): is characterized as the number dislocations of crystal per unit area of crystal structure, was determined with the help of equation [24]:

$$\delta = \frac{15\varepsilon}{a\,D}(lines/cm^2) \tag{2.14}$$

were a is the lattice constant along the a−axis. Moreover, the stacking faults (SF) , which is a type of defect that characterize the disordering of crystallography planes, was calculated using the following equation [25] :

$$SF = \frac{2\pi^2\beta}{45\sqrt{3}\,tan\theta} \times 100\% \quad (2.15)$$

Such the result was explained depend on the lattice mismatch (Δ), which can be calculated by using the formula [26]:

$$\Delta = \frac{a_u - a_s}{a_u} \times 100\% \quad (2.16)$$

Where a_u is the lattice constant of upper layer and a_s is the lattice constant of the substrate layer.

2.1.3 Crystallography:

A crystalline solid consists of repeating patterns of atoms in three dimensions of a crystal lattice. The basic repeating structures of the smallest unit volume, which is defined as a unit cell. The crystals are made of atomic planes that are spaced d apart. However can one determine many atomic planes each with different d lattice spacing [27], of a set of planes that are called Miller indices hkl were used present portion of unit cell are the multiplicative inverse of intercept of the plane with axis in direction of unit cell [28]. The different basic atomic structures of crystalline produce a set of periodic conditions. There are seven evident structures of obtained fourteen different 3-dimentional configurations. These different atomic are arrangements are shown by the set of parameters, the lattice constants a , b and c with α , β and γ of the angles between them. These configurations are called Bravies lattice and represented in Table 2.2 below. which their group of Bravies is classified into several types that depend on structure characterization for combined of fourteen Bravies lattices, were as the orientation of the plane is supplied by given the plane intersects of the solids crystallography axis. The miller indices (hkl) provide the set of numbers that are calculated from the plane of surface.

Table 2.2. The 3D Bravies lattice for solid state materials and their conditions.

Crystal structure	Conditions	Number of Bravies Lattice
Cubic	$a_1=a_2=a_3$ $\alpha=\beta=\gamma=90^0$	3
Hexagonal	$a_1=a_2\neq a_3$ $\alpha=\beta=90^0$, $\gamma=120^o$	1
Trigonal	$a_1=a_2=a_3$ $\alpha=\beta=\gamma<120^o\neq90^0$	1
Tetragonal	$a_1=a_2\neq a_3$ $\alpha=\beta=\gamma=90^0$	2
Orthorhombic	$a_1\neq a_2\neq a_3$ $\alpha=\beta=\gamma=90^0$	4
Monoclinic	$a_1\neq a_2\neq a_3$ $\alpha=\beta=90^0\neq\gamma$	2
Triclinic	$a_1\neq a_2\neq a_3$ $\alpha\neq\beta\neq\gamma\neq90^0$	1

2.1.4 Derivation of the Spacing Interplanar of Hexagonal Lattice:

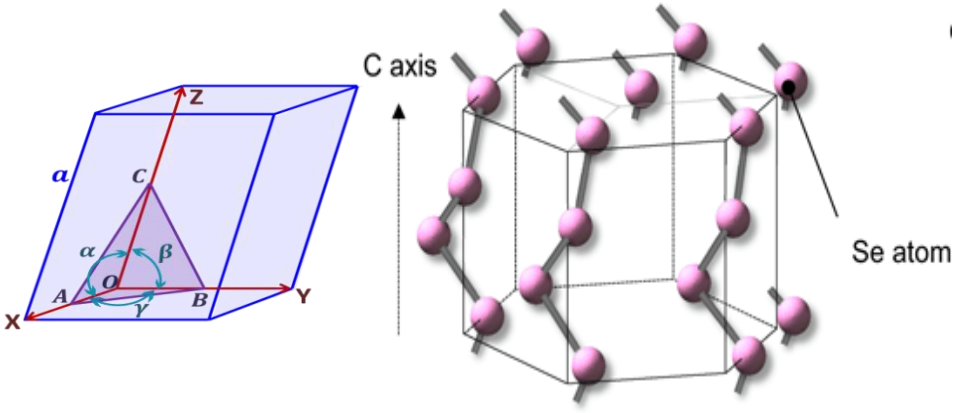

Fig. 2.3: The hexagonal lattice structure

The parameter of hexagonal structure is an angle between basic vectors a and b is 120° that given as:

$$a = b \neq c$$

$$\alpha = \beta = 90^o$$

$$\gamma = 120^o$$

With using to help the triclinic equation [28] to confined the interplanar spacing:

$$\frac{1}{d_{hkl}^2} = \frac{1}{[1+2\cos(\alpha)\cos(\beta)\cos(\gamma)-\cos^2(\alpha)-\cos^2(\beta)-\cos^2(\gamma)]} \times \left[\frac{h^2\sin^2(\alpha)}{a^2} + \frac{k^2\sin^2(\beta)}{b^2} + \frac{l^2\sin^2(\gamma)}{c^2} + \frac{2hk}{ab}(\cos(\alpha)\cos(\beta) - \cos(\gamma)) + \frac{2kl}{bc}(\cos(\beta)\cos(\gamma) - \cos(\alpha)) + \frac{2lh}{ca}(\cos(\gamma)\cos(\alpha) - \cos(\beta))\right] \quad (2.17)$$

Which substitution the condition of the hexagonal structure to becomes:

$$\frac{1}{d_{hkl}^2} = \frac{1}{[1+\cos^2(120)]} \times \left[\frac{h^2+k^2}{a^2} + \frac{l^2\sin^2(120)}{c^2} + \frac{2hk}{a^2}(-\cos(120))\right] \quad (2.18)$$

$$\frac{1}{d_{hkl}^2} = \frac{1}{\left[1+\frac{1}{4}\right]} \times \left[\frac{h^2+k^2}{a^2} + \frac{l^2\times\frac{3}{4}}{c^2} + \frac{2hk}{a^2}\left(\frac{1}{2}\right)\right] \quad (2.19)$$

Where have a result:

$$\frac{1}{d_{hkl}^2} = \frac{4}{3}\left(\frac{h^2+hk+k^2}{a^2}\right) + \frac{l^2}{c^2} \quad (2.20)$$

2.2 Optical Properties:

The optical properties of solids play an important role in the design and development of applications in photonics and optoelectronics. The essential optical properties can be explained using absorption coefficient, band gap theory, band overlapping, dielectric dispersion and other important properties that will be discussed in this chapter.

2.2.1 Optical Spectro-Photometry:

Optical spectro-photometry is a non-destructive method of investigation into the electrical and optical properties of materials [29]. It is defined as science that gives information about the interaction of optical electromagnetic radiation with materials. That involve interactions the splitting of electromagnetic radiation into constituent wavelengths (λ) such as microwaves, infrared, visible light and other wave with different frequencies (v). The waves interactions can be classified into absorption, reflection and transmission. By considering a light beam of electromagnetic waves of a single frequency entering of medium from a vacuum. In fig.2.4 [30], we show the transmitted, reflectance and absorbance of incident rays on an optical medium.

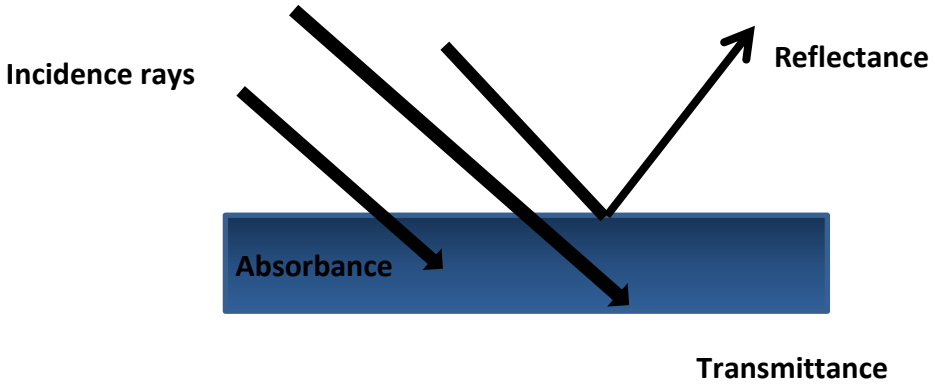

Fig. 2.4: The transmittance, reflectance and absorbance of a light incident on the optical material.

From the fig.2.4, the incident beam may reflect on the front surface or propagate through the medium to reach back surface. This back surface beam may be reflected or transmitted outside the medium. In the different types of interaction, the incident light beam consists of photons with energy (E) equal to [31]:

$$E = h\,v = \frac{hc}{\lambda} \qquad (2.21)$$

Where E is photon energy, h is Plank's constant, v is frequency, c is the speed of light and λ is wavelength. The Reflection cause for reduction of light wave velocity and refers to bending of light beams at interfaces that can be described by Snell's law of refraction [32]:

$$n_1 \sin\theta_1 = n_2 \sin\theta_2 \qquad (2.22)$$

where θ_1 and θ_2 are the angles of incidence and refraction, respectively, of a ray crossing the interface between two media with refractive indices of n_1 and n_2.

2.2.2 Absorption of Light in Material:

The interaction of energetic photons with the optical medium splits light into three types: transmitted, reflected and absorbed. The most attenuated phenomenon is the absorption, Which will happen when light completely propagates into the medium. It means the frequency of the light is resonant, exciting an electron from the valence band to the conduction band. The light absorption of the material can be calculated from the absorption coefficient (α), which is a measure of the rate of decrease of light intensity when incident into the material by using the following relation:

$$\alpha = \frac{A}{d} \qquad (2.23)$$

Where α is absorption coefficient (cm^{-1}), A is the absorbance intensity and d thickness (cm) of the sample. Consider the light beam are propagated in z-direction and the intensity at point z is $I(z)$ then the decrease of intensity of light in an incremental slice of thickness (dz) is [33] :

$$dI = -\alpha I(Z)dZ \qquad (2.24)$$

The above equation is integrated to obtaining Beer's law:

$$dI = I_o e^{-\alpha Z} \quad (2.25)$$

Where I_o is optical intensity at Z=0, $\alpha\ is$ the absorption coefficient. The transmittance of light for two parallel surfaces is [34]:

$$T = (1 - R_1)(1 - R_2)e^{-\alpha d} \quad (2.26)$$

The transmittance of multilayer film is expression of [34]:

$$T = \frac{(1-R_1)(1-R_2)e^{-\alpha d}}{1-R_1R_2e^{-2\alpha d}} \quad (2.27)$$

Thus, the absorption coefficient $\alpha(hv)$ for samples deposition on glass substrate, can be calculated as:

$$\alpha = -\frac{1}{d}\ln\left(\frac{T}{(1-R_{glass})(1-R_{sample})}\right) \quad (2.28)$$

2.2.3 Band Gap Calculation:

Optical absorption spectroscopy is used to obtain the band gap and band structure of thin films. Analysis of optical absorption spectra is the most productive technique for understanding the energy band diagram of both amorphous and crystalline materials. From the meaning of the optical transition induced in the absorption process, which is considered the optical band gap value. Tacu's equation measures the relationship between the absorption coefficient and the incident photon energy. The formula of Tauc's equation is given by [35]:

$$(\alpha hv)^m = B\left(hv - E_g\right) \quad (2.29)$$

were $(h\nu)$ is the incident photon energy, (E_g) is the energy band gap, (B) the absorption constant that depends on transition probability and (m) is index that characterizes the optical absorption and is numerically equal to 2, 1/2, 1/3 and 3/2. There numbers relate to direct allowed, indirect allowed, direct forbidden and indirect forbidden transitions, respectively.

In order to explain how to get the tauc's equation, we start from the absorption coefficient (α)

$$\alpha = \frac{(\hbar\omega)(transition\ probability/volume\ time)}{total\ intensity} \tag{2.30}$$

$$\alpha = \frac{(\hbar\omega)S_{i\to f}}{I} \tag{2.31}$$

which $\hbar$ is Plank's constant $=h/2\pi$, ω is the angular frequency of a photon and $S_{i\to f}$ is the quantum mechanical transition rate from an initial state to a final state where defined as:

$$S_{i\to f} = \frac{2\pi}{\hbar}|M|^2\rho(\hbar\omega) \tag{2.32}$$

$\rho(\hbar\omega)$ is the density of state and M is a matrix element describing the perturbation caused by light, where $\rho(\hbar\omega)$ integral formula is shown as:

$$M = \int \psi_f{}^*(r)H'\psi_i{}^*(r)d^3r \tag{2.33}$$

H' is the interaction perturbation, $\psi_i{}^*$ the initial state, $\psi_f{}^*$ the final state and r is electron position, and the external perturbation can be expressed by:

$$\acute{H} = \frac{e}{m_o}\vec{A}.\vec{P} \tag{2.34}$$

P is the electron momentum, which is evaluated as $i\hbar\,\partial$, m_o the free electron mass and $\vec{A}$ is the potential vector where it:

$$\vec{A}(r,t) = A_o e^{i(K_r - wt)} \quad (2.35)$$

The energy E expressed of charge particle which is shifted in the range by $-PE$ that shows as:

$$E(r)_{photon} = E_o e^{iK.r} \quad (2.36)$$

The electric dipole (P) is:

$$P = -er \quad (2.37)$$

Referring to the previous perturbation relation, and suitable to displaying as:

$$\acute{H} = -P.E \quad (2.38)$$

Then,

$$\acute{H} = e\, E_o\ \ e^{iK.r}.r \quad (2.39)$$

During to Bloch theorem, which gets the wave as follows functions expression as below:

$$\psi(r) = \frac{1}{\sqrt{V}} u(r) e^{iK.r} \quad (2.40)$$

Can be applied to the initial and final states, where that V is volume normalization, K state wave function and $u(r)$ the perturbation functions, these parameters are used to prepare M as:

$$M = \frac{c}{V} \int {u_f}^*(r)\, e^{-iK_f.r} E_o r\, e^{iK.r} {u_i}^*(r) e^{iK_i.r} d^3r \quad (2.41)$$

For solving the above integral, applies first the Bloch's theorem. The density of energy d(E), then acts function as a conservation in momentum.

$$D(E)dE = 2\, D(k)dk \quad (2.42)$$

Here d(k) denotes the density function of moment and factor 2 for electron spin state.

$$D(\hbar\omega) = \frac{2\,d(E)}{dE/dk} \tag{2.43}$$

According to the definition of D(E), the number of states per unit volume in momentum space, So that,

$$D(k)dk = \frac{1}{2\pi^2} \cdot 4\pi\, k^2 dk \tag{2.44}$$

$$D(k)dk = \frac{k^2}{2\pi^2} dk \tag{2.45}$$

And so, equ.2.39 becomes

$$D(\hbar\omega) = \frac{1}{2\pi^2} \left(\frac{2m^*}{h^2}\right)^{2/3} E^{1/2} \tag{2.46}$$

Here, $\hbar\omega$ is the energy and m^* is the effective mass with the following conservation of energy equation:

$$\hbar\omega = E_g + \frac{(\hbar \mathrm{k})^2}{2M} \tag{2.47}$$

E_g is the energy gap and M the reduced electron – hole mass, which evaluated as:

$$\frac{1}{M} = \frac{1}{m_e{}^*} + \frac{1}{m_{hole}{}^*} \tag{2.48}$$

The photon energy divided two regions above $\hbar\omega$ and below energy gap, So that presented the density of state as:

$$D(\hbar\omega) = \begin{cases} \frac{1}{2\pi^2}\left(\frac{2M}{\hbar^2}\right)^{\frac{3}{2}} \left(\hbar\omega - E_g\right)^{\frac{1}{2}} & ,\hbar\omega > E_g \quad (2.49) \\ 0 & ,\hbar\omega < E_g \quad (2.50) \end{cases}$$

The resulting relation between 2.49 and 2.31, which is used to measure and simplify the equ.2.32, then we get:

$$\alpha = B\ \frac{(\hbar\omega - E_g)^{\frac{1}{2}}}{\hbar\omega} \qquad (2.51)$$

$$\alpha\ \hbar\omega\ \propto\ (\hbar\omega - E_g)^{\frac{1}{2}} \qquad (2.52)$$

Here power factor $\frac{1}{2}$ denotes the direct transition bad gap, instead of this case. Generally,

$$\alpha\ \hbar\omega\ \propto\ (\hbar\omega - E_g)^{m} \qquad (2.53)$$

From the representation of $(\alpha E)^{\frac{1}{m}} - E$ plot and by obtaining the linear fitting, m is the integer factor. the intercept of the E – axis becomes the energy gap for determined thin films.

2.2.4 Direct and Indirect Transitions:

The direct and indirect character of the band gap transition is an interesting parameter of semiconductors for optoelectronic devices. In the fig.2.5 [36] , it can be observed that the energy band gap range of the valence bands and conduction band is consistent with the minimum energy state in conduction bands and the maximum energy state in valence bands.

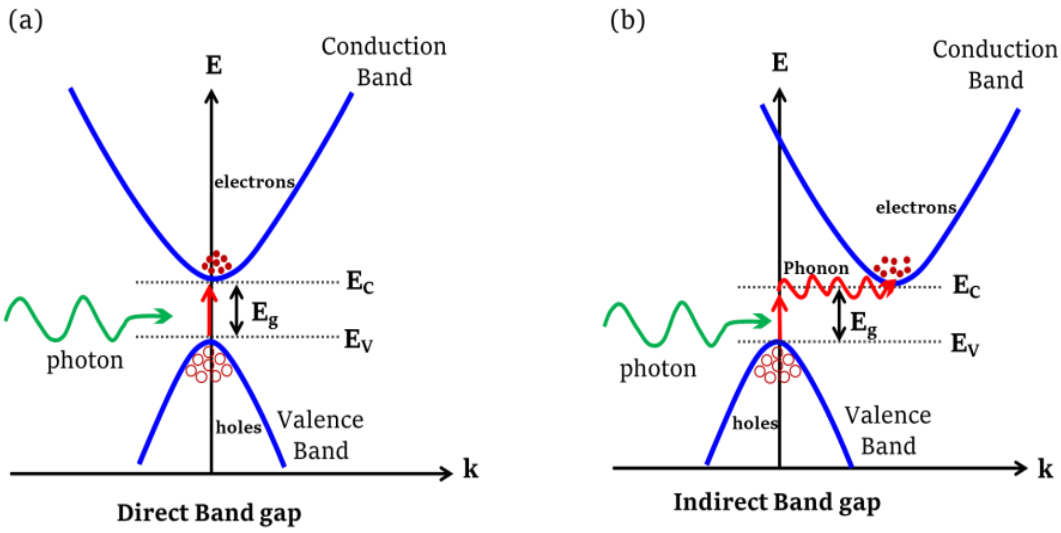

Fig. 2.5: Incident photons cause solid Interbrand (a)direct transition and (b)indirect transitions

A direct band gap forms if the conduction band minimum is at the same point in *k*-space as the valence band maximum, both corresponding to the same momentum point in the center of the Brillouns zone. An indirect band gap is assigned to the valence band maximum, which is misaligned with the conduction band minimum in momentum.

2.2.5 Band Tails:

Band tails are characterized by bands that appear more in an amorphous semiconductor, where localized electronic state that extended to band gap that below the conduction band (CB) or above the valence band (VB), as their simplified band diagram shown in fig.2.6. That tail state as consequence of the disorder [37].

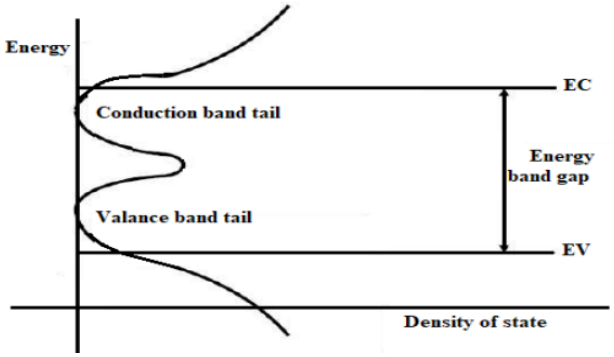

Fig. 2.6: Energy band position

Deep describes the absorption coefficient configuration at low frequency, were a new process can occur associated with free carriers. A photon excited an electron from an occupied state in valence band sate of to an unoccupied state conduction band. Thus, it a transition process is called inter brand transition.

Due to an impurity or defect present in the band structure of amorphous semiconductors more than crystalline, their large density of localized states leads to a high density of positively and negatively charged traps that lead to a decrease in the mobility of carriers [38]. Consider a p-type degenerate semiconductors with a valence band perturbation above Fermi level [39].

For this reason, the final state density N_f of conduction tails relations of the initial state N_i are as follow:

$$N_f = N_i e^{E/E_o} \tag{2.54}$$

Which E_o: the dimension energy of density state and E: energy state, derived from the absorption coefficient definition used to derive the relationship between the band tail and α coefficient: ξ

$$\alpha(hv) = A \int_{\xi_o}^{hv-\xi_o} |E_v|^{1/2} e^{E/E_o} \, dE \tag{2.55}$$

Which A is constant. let $y = \frac{hv-E}{E_o}$ with substituted y in the integral:

$$\alpha(hv) = -A(\frac{hv}{E_o})(E_o)^{3/2} \int_{\xi_o}^{hv-\xi_o} y^{\frac{1}{2}} e^{-y} dy \quad (2.56)$$

If $hv \gg E_o$, the lower limit of the integral approach is ∞ and the integral is divided into two steps $(\infty - 0)$ and (0-$\frac{\xi_o}{E_o}$) to get:

$$\alpha(hv) = -A \exp(\frac{hv}{E_o})(E_o)^{3/2} \left[\frac{1}{2}(\pi)^{\frac{1}{2}} - \int_0^{\frac{\xi_o}{E_o}} y^{\frac{1}{2}} e^{-y} dy\right] \quad (2.57)$$

The slop of a semi-logarithm curve is as follows:

$$\left[\frac{\partial \ln(\alpha)}{\partial(hv)}\right]^{-1} = E_o \quad (2.58)$$

Then, the reciprocal relation:

$$\frac{1}{E_o} = \frac{\partial \ln(\alpha)}{\partial(hv)} \quad (2.59)$$

Integrating the Egu.2.59 yields

$$\frac{1}{E_o} \int \partial(hv) = \int \partial \ln(\alpha) \quad (2.60)$$

$$\ln(\alpha) = \ln(\alpha_o) + \frac{hv}{E_o} \quad (2.61)$$

The result from the plot $\ln(\alpha)$ with respect to the energy (E) is that the interband energy can be determined from the slop.

2.2.7 Dielectric Constant and Dielectric Refraction Index:

The dielectric constant has significance for optical properties, which consists of the real part that is responsible for the ability to store the electrical energy in the material, while the imaginary part represents the damping in the wave and dissipation of energy. The other optical parameters are the refractive index (n) which it expresses the light interaction and its travel in the medium, A complex refractive index is a combined quantity involves of a real part that displays the refractive index (n) and an imaginary part that where gives the extinction coefficient (k) for material. The complex refractive index expression of the combination of the real and imaginary parts with the optical wave length derivative by dispersion equation [40], is shown as follows:

$$\widetilde{N}_{complex} = n(\lambda) + ik(\lambda) \tag{2.62}$$

$$= (\varepsilon_r + \varepsilon_{im})^{\frac{1}{2}} \tag{2.63}$$

n is the refractive index, k is the extinction, ε_r is the real dielectric constant and ε_{im} the imaginary constant. The dielectric is the ratio of material permittivity preparation to the vacuum permittivity, for that to exhibit the dielectric constant equation and identified the combination between the extinction coefficient and the absorption coefficient, we assume an electric field in the x-direction travelling in z-axis and included the incident and reflected waves,

$$\vec{E}_x = E_o e^{i(kz-\omega t)} \tag{2.64}$$

E_o is the amplitude at $z = 0$, k is wave vector and ω is the angular frequency. The following formula examined the relation between the k and ω:

$$k = \frac{2\pi}{(\frac{\lambda}{n})} \tag{2.65}$$

It may be generalized with the help of complex refractive index.

$$k = \frac{\omega}{c}\ \widetilde{N}_{complex} \tag{2.66}$$

when the electric field involved incident and reflected waves travelling through the z-axis, resulting in:

$$\vec{E}_x = E_o e^{i(\frac{\omega t}{c}\widetilde{N}_{complex} - \omega t)} \tag{2.67}$$

$$\vec{E}_x = \vec{E}_1 e^{i(\frac{\omega z}{c} - \omega t)} + \vec{E}_2 e^{-i(\frac{\omega z}{c} + \omega t)} \tag{2.68}$$

$$\vec{E}_o = \vec{E}_1 + \vec{E}_2 \tag{2.69}$$

which $\vec{E}_o, \vec{E}_1 and\ \vec{E}_2$ are described by the continuity equation for H_y , the tangential magnetic field component at the dielectric surface.

From definition, Maxwell's equations[41]:

$$\nabla \times \vec{E} = -\frac{\mu}{c}\frac{\partial \vec{H}}{\partial t} = i\frac{\omega\mu}{c}\frac{\partial \vec{H}}{\partial t} \tag{2.70}$$

$$\frac{\partial \vec{E}_x}{\partial z} = i\ \frac{\omega\mu}{c}\frac{\partial \vec{H}}{\partial t} \tag{2.71}$$

From referring to equation 2.58 and its derivative relative to the z – axis:

$$E_o k = E_1\ \frac{\omega}{c} - E_2\ \frac{\omega}{c} = E_o\ \frac{\omega}{c}\ \widetilde{N}_{complex} \tag{2.72}$$

The result of equation 2.72 after simplifying and rearrangement is given:

$$E_1 + E_2 = E_o\ \widetilde{N}_{complex} \tag{2.73}$$

By solving equations 2.69 and 2.73, we get:

$$E_2 = \frac{1}{2}E_o\ (\ 1 - \frac{\omega}{c}\ \widetilde{N}_{complex}\ ) \tag{2.74 (a)}$$

$$E_1 = \frac{1}{2} E_o \left(1 + \frac{\omega}{c} \widetilde{N}_{complex} \right) \quad (2.74(b))$$

Which the reflected of the normal incident are getting as the follow[42]:

$$R = \left| \frac{E_2}{E_1} \right|^2 \quad (2.75)$$

Simplifying equation 2.75 through substation, the equations 2.74 (a) and 2.74 (b):

$$R = \left| \frac{1 - \frac{\omega}{c} \tilde{N}_{complex}}{1 + \frac{\omega}{c} \tilde{N}_{complex}} \right|^2 \quad (2.76)$$

Substituting equation 2.52 in the equation 2.76 we get:

$$R = \frac{1 + n^2 - 2n + k^2}{1 + n^2 + 2n + k^2} \quad (2.77)$$

Consider the medium had strong absorption. In addition, the large values of n and k compared to unity terms (n >> k >> 1), the equation 2.77 yield to:

$$R = \frac{n^2 - 2n + k^2}{n^2 + 2n + k^2} \quad (2.78)$$

That obtained to,

$$Rn^2 + 2Rn + Rk^2 = n^2 - 2n + k^2 \quad (2.79)$$

$$(R - 1)n^2 + 2(R + 1)n + (R - 1)k^2 = 0 \quad (2.80)$$

Solving by the general law ($x = \frac{-b \pm \sqrt{b^2 - 4ac}}{2a}$) to existing:

$$n = \frac{-(2R+1) \pm \sqrt{4(R+1)^2 - 4(R-1)(R-1)k^2}}{2(R-1)} \quad (2.81)$$

For more to simplify we get,

$$n = \frac{-(R+1)}{(R-1)} \pm \sqrt{\left(\frac{R+1}{R-1}\right)^2 - k^2} \quad (2.82)$$

Then, the roots become:

$$n_1 = \frac{-(R+1)}{(R-1)} + \sqrt{\left(\frac{R+1}{R-1}\right)^2 - k^2} \quad (2.83\ (a))$$

$$n_1 = \frac{-(R+1)}{(R-1)} - \sqrt{(\frac{R+1}{R-1})^2 - k^2} \quad (2.83(b))$$

That well an identified the effective dielectric constant (ε_{eff}) which presented in the dielectric refractive index (n) as observed:

$$n = \sqrt{\varepsilon_{eff}} \quad (2.84)$$

In terms of the equation 2.72 becomes:

$$\sqrt{\varepsilon_{eff}} = \frac{-(R+1)}{(R-1)} \pm \sqrt{(\frac{R+1}{R-1})^2 - k^2} \quad (2.85)$$

Similar to that, the ε_{eff} roots are getting:

$$\varepsilon_{eff_1} = \frac{-(R+1)}{(R-1)} + \sqrt{(\frac{R+1}{R-1})^2 - k^2} \quad (2.86(a))$$

$$\varepsilon_{eff_2} = \frac{-(R+1)}{(R-1)} - \sqrt{(\frac{R+1}{R-1})^2 - k^2} \quad (2.86(b))$$

To get the dielectric constant (ε) formula for derivation with respect to the complex refractive index ($\widetilde{N}_{complex}$):

$$\widetilde{N}_{complex} = \sqrt{\mu\varepsilon} \quad (2.87)$$

Were, the non –magnetic material $\mu = 1$. then,

$$\widetilde{N}_{complex} = \sqrt{\varepsilon_{eff}} \quad (2.88)$$

The dielectric constant is displayed as a complex number, which can be written as:

$$\varepsilon_{eff} = \varepsilon_r + i\varepsilon_{im} \quad (2.89)$$

Here, ε_r is the real part and $\varepsilon_{im}$is the imaginary part of the dielectric constant.

Substituting equation 2.53 in 2.88 to become:

$$(\widetilde{N}_{complex})^2 = \varepsilon_{eff} = (n + ik)^2 \quad (2.90)$$

$$\varepsilon_{eff} = n^2 - k^2 + i2nk \quad (2.91)$$

Through compared the equation 4.91 and 4.89 to exhibit as:

$$\varepsilon_r = n^2 - k^2 \quad (2.92)$$

$$\varepsilon_{im} = 2nk \quad (2.93)$$

To introduce the relation between k and α, we assume that an electromagnetic wave propagates in the z – direction of medium with an electric field.

$$\vec{E}(z,t) = E_o e^{i(kz-\omega t)} \quad (2.94)$$

which E_o is the amplitude at $z = 0$ and t=0, k is the wave vector and ω is the frequency. Significant to observe the relation between the extinction coefficient (k) and wave length (λ):

$$k = \frac{2\pi}{(\frac{\lambda}{\widetilde{N}})} \quad (2.95)$$

In order to add equations 2.53, 2.56, 2.95 and 2.96 to get:

$$k = \frac{\omega}{c}(n + ik) \quad (2.97)$$

$$\vec{E}(z,t) = E_o e^{i(\frac{\omega nz}{c}-\omega t)} e^{-\frac{kz\omega}{c}} \quad (2.98)$$

The optical intensity of a light wave is proportional to the square of the electric field which $I \propto EE^*$, [43] hence to:

$$I \propto e^{-i(\frac{\omega kz}{c})} \tag{2.99}$$

Where the above 2.89 equation compared with 2.4 become:

$$2\ \frac{k\omega}{c} = \alpha = \frac{4\pi k}{\lambda} \tag{2.100}$$

Thus,

$$k = \frac{\lambda\alpha}{4\pi} \tag{2.101}$$

2.2.7 Drude-Lorentz Model:

In order to form the dielectric constant measured, the imaginary part spectra ε_i which it is possible to analyze with the help of effective oscillator models [44]. This model is applied to supply compressive polarization.

The dielectric of solid atoms can be as a coalescing of oscillation. Considering oscillation by the AC electric field of a wave polarized along the x-axis, which concludes the oscillations of free electron where the motion relation is described by:

$$m_o \frac{\partial^2 x}{\partial t^2} + m_o y \frac{\partial x}{\partial t} + m_o {\omega_o}^2 x = eE \tag{2.102}$$

Here m_o the electron mass, x the displacement, y is the damping factor, e the electron charge and E the electric field. The equation identified the damped side of acceleration and the factor was restored. In addition to the driving force.

In terms, the electrons contact the incident light electric field with frequency, to show the electric field as:

$$E(t) = E_o \cos(\omega t + \varphi) - E_o R_o(\exp(-i\omega t - \varphi)) \quad (2.103)$$

Where E_o the electric field amplitude and φ the light phase. The AC signal of the electric field produces the oscillation of thought form:

$$x(t) = x_o Re(\exp(-i\omega t - \varphi_o)) \quad (2.104)$$

Here x_o and φ_o with the complete electric component electric displacement amplitude, the equation of motion yields to substitution $E(t)$ and $x(t)$ in equation 4.92 to becomes:

$$-m_o\omega^2 x_o e^{-i\omega t} - m_o y\omega x_o e^{-i\omega t} + m_o {\omega_o}^2 x_o e^{-i\omega t} = -eE_o e^{-i\omega t} \quad (2.105)$$

Then, by making a re-arrangement of the previous equations (2.105) with divided over $e^{-i\omega t}$, supply the displacement amplitude as:

$$x_o = -\frac{eE_o/m_o}{{\omega_o}^2 - \omega^2 - i\gamma\omega} \quad (2.106)$$

The resultant of frequency variants of the dipole moment $P(t)$ perform in the resonant polarization induction, which the polarization of dipole moment per unit volume presented as:

$$P_{resonant} = Np = -N_{ex} \quad (2.107)$$

From substitution x_o in $P_{resonant}$:

$$p_{resonance} = \frac{Ne^2}{m_o} \frac{1}{{\omega_o}^2 - \omega^2 - i\gamma\omega} E \quad (2.108)$$

Here, N is the number of atoms per unit volume. Where the relation described the causes of the maximum polarization equation of the material frequencyω_o. The interesting parameter is the electric displacement D of solids, which it depend on polarization and the electric displacement as seen below:

$$D = \varepsilon_o E + P \tag{2.109}$$

Another cause of polarization when oscillation is ignored, is if $\omega \neq \omega_o$ the polarization involvesthe resonance and non-resonance:

$$D = \varepsilon_o E + P_{non-resonance} + P_{resonance} \tag{2.110}$$

In the non-resonance part, which depends on the susceptibility χ as expressed in the following:

$$P_{non-resonance} = \varepsilon_o \chi E \tag{2.111}$$

The displacement D received:

$$D = \varepsilon_o E + \varepsilon_o \chi E + P_{resonance} \tag{2.112}$$

Consider the isotropic material with the same characteristics in all directions to become the electric displacement as:

$$D = \varepsilon_o \varepsilon_r E \tag{2.113}$$

which ε_r is the relative dielectric constant when the equation 2.112 substations into 2.113 with applied the resonant polarization. Thus, the dielectric constant exhibits:

$$\varepsilon_r(\omega) = 1 + \chi + \frac{Ne^2}{\varepsilon_o m_o} \frac{1}{{\omega_o}^2 - \omega^2 - i\gamma\omega} \tag{2.114}$$

The two terms of relative dielectric constant ε_r give the real and imaginary parts as:

$$\varepsilon_1(\omega) = 1 + \chi + \frac{Ne^2}{\varepsilon_o m_o} \frac{{\omega_o}^2 - \omega^2}{({\omega_o}^2 - \omega^2) - (\gamma\omega)^2} \tag{2.115}$$

$$\varepsilon_2(\omega) = \frac{Ne^2}{\varepsilon_o m_o} \frac{\gamma\omega}{({\omega_o}^2 - \omega^2) - (\gamma\omega)^2} \tag{2.116}$$

Chapter Three

Experimental Details

This chapter, discusses the experimental methods for the preparation of thin films fabricated as optoelectronic devices by the thermal vapor deposition technique. Particularly, the experimental procedures, cleaning of samples, deposition and characterization of Se, $CdBr_2$ and Se/$CdBr_2$ heterojunction are reported.

3.1 Cleaning the Glass Slides

In this work, we used glass substrates (soda lime; SiO2: Na2O: MgO: CaO). Firstly, we used a clean piece to wash the glass substrate from both sides by distilled water and alcohol, then immersed it in a beaker containing H_2O_2 (hydrogen peroxide) covered with aluminum foil. Second, the beaker is immersed in an ultrasonic resonator. The resonator heats the water till reaching 70^oC while shaking the liquid ultrasonically. In order to remove dusts and contaminates from the surface. Then, tacking the glass slides out to wash them with alcohol, they are then re-immersed in H_2O_2 solution to return into ultrasonic for half an hours at room temperature about 30^oC.

Finally, after heated they were washed well with alcohol and dried gently with glass paper. The slides were also checked to avoid any scratches on the surface, so it was ready for the next process.

3.2 Evaporation Technique and Thin Films Preparation

Vacuum technology is a significant technique for several applications in physics. The target of this thesis, is studying Se/$CdBr_2$ thin films heterojunction which are prepared by thermally deposition by physical evaporation technique (PVD) using VCM 600 V2 desktop vacuum evaporator onto cleaned glass substrate under a vacuum pressure of 10^{-5} mbar. Fig 3.1 represents the configuration of the vacuum evaporation system.

A stainless-steel vacuum chamber (item−1) can be moved up and down. Within the chamber, a heating boat (item−2) such that the substance to be evaporated is placed, and a substrate holder, which is for glass substrate (item−3) is also presented. The desktop system include a power supply that is tuned at a suitable current to reach specific temperature for heating the boat (item−4). In addition, the power given to the system by turning the switch to main power on (item−5), the green light on the left side of the switch on shows the availability of electrical power. The (item−6) of rough pump switch for turning on providing power to primary pump. Item−7 is a heating power control unit (PCU) with a continuing high current AC power supply. In addition, the adjustable shalter is adapted to control the evaporation and a valve switch is used to restore the chamber pressure to its initial state. These are item−8 and item−9 respectively.

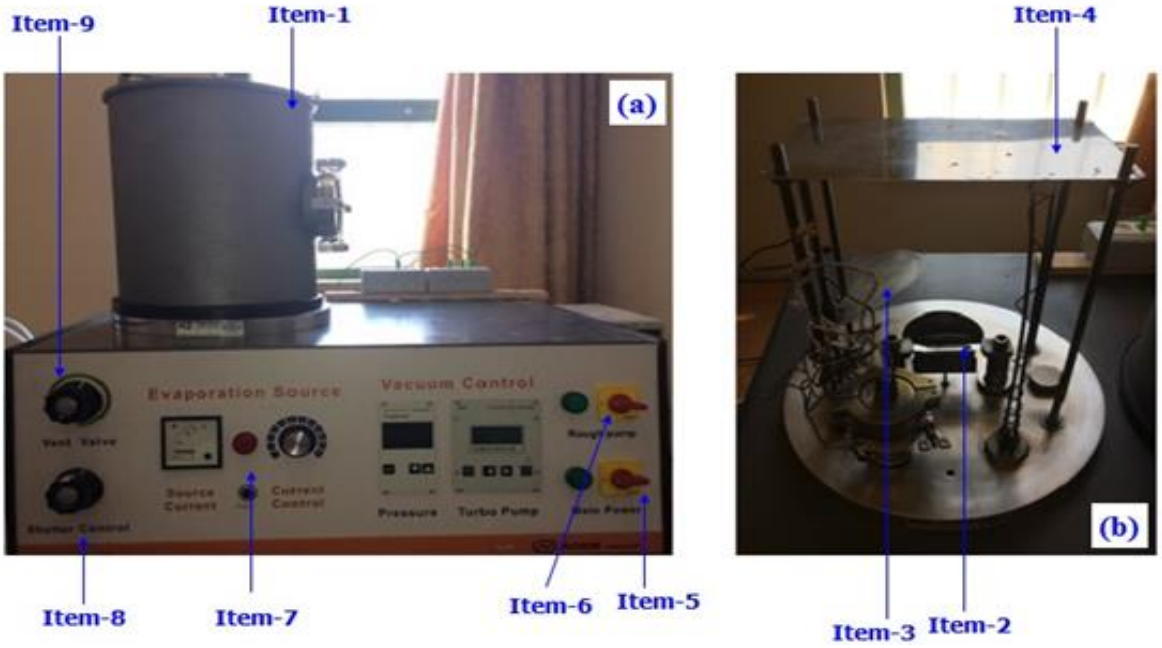

Fig. 3.1: (a) Configuration of thermal evaporation system (b)Inside chamber

During the evaporation process, the first step is to install the of weight of 0.5 grm of high purity Selenium (99.99% $Alfa\ Aesar$) into the evaporation boat. After evacuating the VCM 600 system, the first growth cycle was actualized, resulting in 0.5 μm thick film being deposited on a glass substrate. The schematics and optical images of the produced Se films are shown in Fig.3.2(a) and Fig.3.3(a), respectively. After that, some portions of the Se samples were covered by a TEFLON strip. In order to obtain the covered part which is Se thin films with the rest part being Se/$CdBr_2$ expose part of double thin films. The masked Se sample together with other cleaned glasses are re-installed into the VCM system prior to coating of $CdBr_2$. In this process, 0.5 grm of Cadmium Bromide ($CdBr_2$) (99.99% metal basis Alfa Aesar) are installed into the heating boat. After completing the evaporation cycle, a 0.5 μm thick layer was produced on to Se thin film.

The produced Se, $CdBr_2$ and Se/$CdBr_2$ thin films, the schematic diagram and optical image of these films are presented in Fig 3.2 (a), (b) and (c) and Fig.3.3 (a), (b) and (c) respectively.

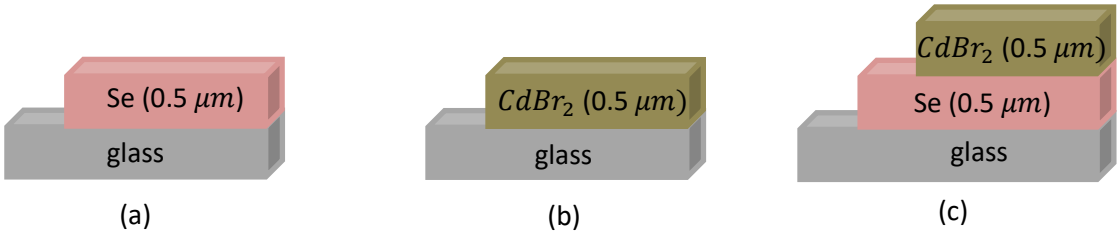

Fig.3.2: Geometrical diagram of (a) glass/Se, (b) glass /$CdBr_2$ and (c) glass/Se/$CdBr_2$ thin films.

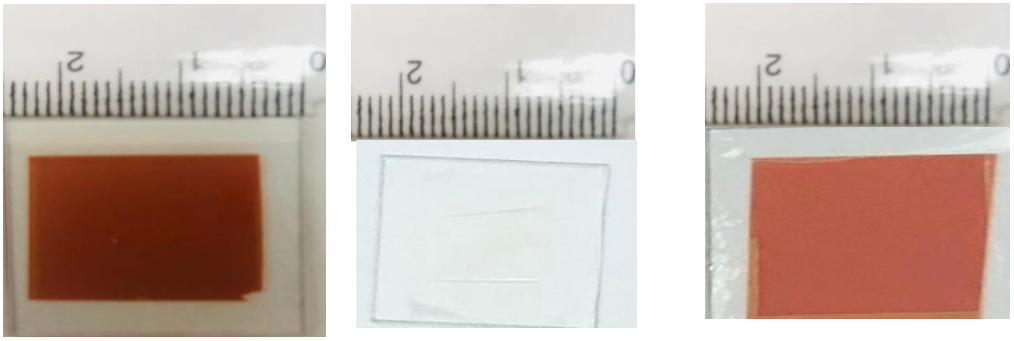

Fig. 3.3: Optical images for (a) glass/ Se, (b) glass/$CdBr_2$ and (c) glass/ Se/$CdBr_2$ thin films.

3.3 Thin Film Analysis:

Having prepared the samples we are ready to study some of the interesting properties like the structural, optical and dielectric properties. By using the hot probe technique, the conductivity type of the samples was explored.

3.3.1 The Hot Probe Technique:

The “hot-probe” technique, which is present in fig. 3.4 was needed to know the thermal conductivity type of Se, $CdBr_2$ and Se/$CdBr_2$ semiconductors. In this experiment, the required equipment is a heater, a standard digital multi-meter (DMM) and wires. By connecting the two wires with the DMM and coupled the positive terminal with the heater, the negative terminal was touched on the surface sample surface. At the contact point, the sample and heater have higher thermal energy than other cooler parts. During heating process, that increases the number of higher energy carriers that diffuse away from the contact point. The majority carries is determined. In practice, a negative voltage was read on the DMM indicated the p-type for Se, $CdBr_2$ and Se/$CdBr_2$ while the positive voltage indicating the n-type for the mentioned films.

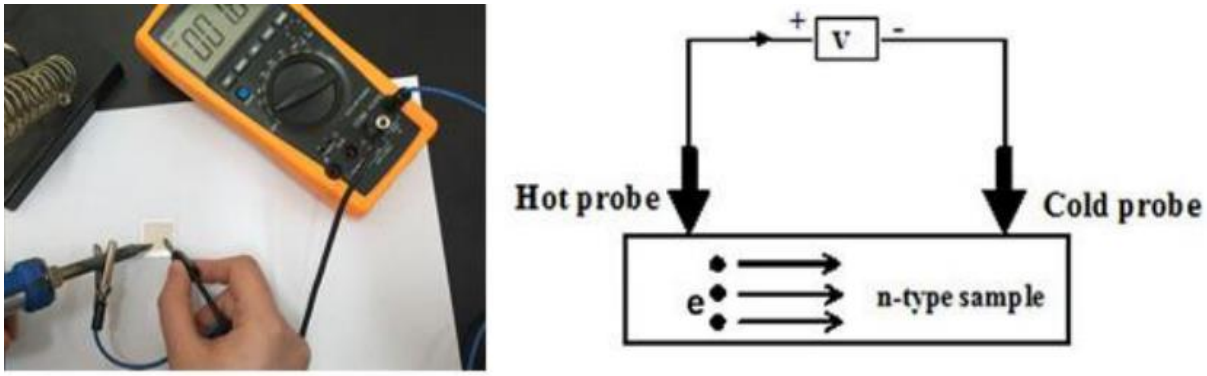

Fig. 3.4: the set -up of hot - probe technique

3.3.2 The X−Ray Diffraction (XRD) Measurement:

The prepared Se 0.5 μm (500 nm), $CdBr_2$ 0.5 μm (500 nm) and Se/$CdBr_2$ 1 μm (1000 nm) films with glass base were analyzed by the Mini Flex-600 X-ray diffraction unit, which is shown in fig. 3.6 to provide information about the crystalline nature. In addition, the “Crysdiff” software packages were used in order to identify the observed peaks. X−ray diffraction is the

most advanced technique, and it is generated by a high intensity monochromatic K_α radiation source. The XRD system shown in Fig.3.5 included a generator of a copper tube of average wavelength of 1.5405 A^o output current of 15 mA and output voltage of 40 KV, a graphite monochromatic, a rotary shutter, a sample holder, a detector and vertical goniometry. The scanning angle (2θ) was in range of $10^o - 70^o$ with the scan speed of 1 deg/min. The diffraction process can be explained by using Bragg equation 2.1. When an X−ray beam is incident on the crystal, the beam is reflected on the upper and lower surfaces, allowing us to determine the path difference of incident wavelengths and then satisfy the Bragg equation.

Fig. 3.5 : the X-ray diffraction system.

3.3.3 Optical Measurement:

The optical analyses of Se, $CdBr_2$ and $Se/CdBr_2$ were characterized by using a Thermo Scientific Evolutions 300 ultraviolet–visible light spectrophotometer, which is shown in fig. 3.6. The measured data is the percentages of transmitted (T%) and reflected (R%) light by using the vision software packages. The R% and T% were calculated at room temperature in the ultraviolet, visible and near infrared ranges of the electromagnetic spectrum. In addition, at normal incidence 15^o with a wavelength range of 300 – 1100 nm and scanning speed of 1200 nm/min.

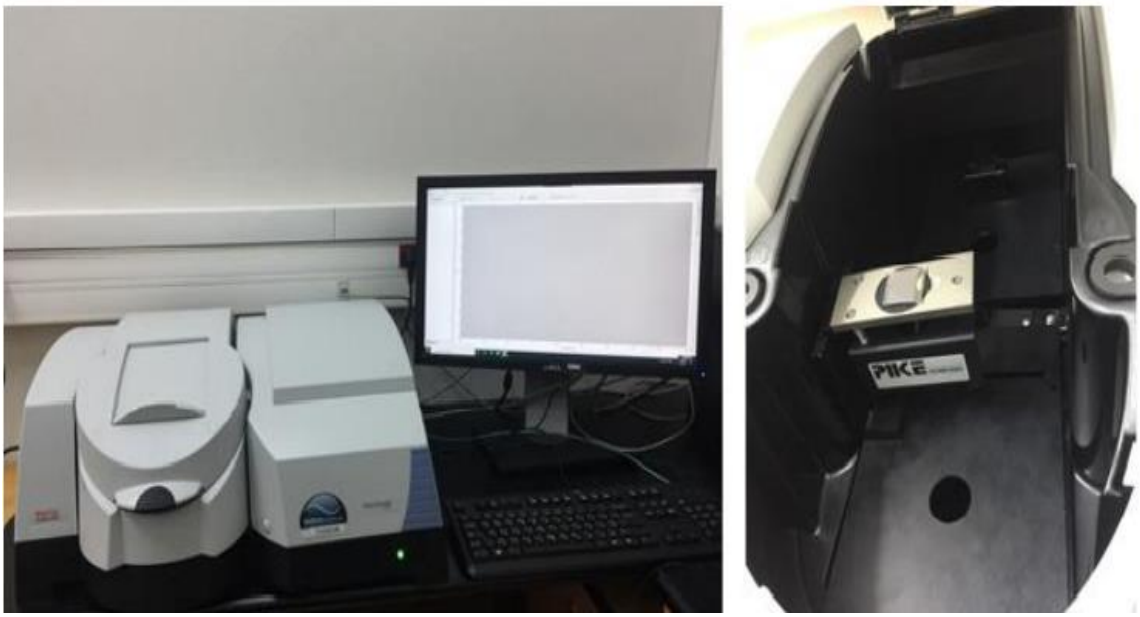

Fig. 3.6: the optical spectrometer equipment

Chapter Four

Results and Discussions

4.1 Structural Analysis:

4.1.1 Structural Transformation in Selenium Thin Films:

Selenium is known for its allotropic structures. It can be cubic, amorphous selenium (a−Se), rohmedral, monoclinic (α −, $\beta-$, γ − Se) and hexagonal (tetragonal) (h−Se) [45]. Therefore, selenium thin film has the ability to show a transition from an unstable structural phase to a crystalline stable phase. The trigonal Se (t-Se) configuration is composed of helical polymeric chains with trans–configurations of Se atoms in which the neighbor's atoms form single covalent bonds, while the chains interacts by Vander walls forces. In addition, t-Se is the most stable allotrope with the least reactive solid properties [46]. The trigonal Se is characterized by infinite helical chains and (α -, $\beta-$, γ − Se) is characterized by Se_8 rings of different packing geometries [47]. Moreover, the hexagonal Se crystal consists of parallel infinite chains of Se. Here, Se atoms are arranged in helical form along the c-axis.

In order to observe the stability and structural properties of Se thin films, a 0.5 μm thick layer of Se film was deposited on the glass substrates. Then a 0.5 μm thick with $CdBr_2$ was deposited on to Se film. The amorphous structure forms of Se is weekly bonded and consist of very short, regular chains with bond angles being slightly distorted. Thus, it has a large number of unsaturated bonds [48,49].

In a previous work, it was concluded that the crystallization process starts at a high temperature of about 132^oC, which makes the phase change temperature exhibit convincing agreement and

confirm the monoplanes due to the small crystallite size and the additional strain broadening [50].

In another work, the amorphous nature of Se (a-Se) solid is affected under high pressure due to volume expansion generated by the high density of metastable selenium that can be converted to stable Se to minimize the internal energy [51]. For significant observation of changes in crystalline structure of Se thin film we waited four weeks after preparations. The measurement by that time showed that Se making a phase transition from amorphous structure to polycrystalline after four weeks of preparations.

The structural properties of fresh Se and Se after four weeks of preparation films were recorded by X−ray diffraction. The XRD patterns for the same films were recorded weekly until the obtained measurements became consistent.

The resulting XRD patterns for the films are shown in Fig.4.1. Three sharp diffraction patterns were observed after 4 weeks. In order to detect the structural properties of Se films the XRD patterns were analyzed with the help of “Crysdiff” "software packages. As seen from the fig.4.1 for the fresh Se and Se after four weeks, the fresh Se films are showing no peaks, indicating the amorphous nature of the films. As illustrated in inset-1, these films show orange color. While the Se after four weeks shows one major peak centered at $2\theta = 23.85^{o}$ and two minor peaks around $2\theta = 41.55^{o}$ and $2\theta = 52.5^{o}$. In accordance with the “Crysdiff” analyses the peaks can be assigned to hexagonal Se whose lattice parameters and space group are (a=4.31 Å and c=3.48 Å) and P312, respectively. As also seen from inset-2 of Fig.4.1, the orange Se inverts color and becomes grey.

As shown in Fig.4.2 hexagonal crystallize Se structure. In contrast to its amorphous phase, which consists of random chains with twofold coordinated Se atoms, hexagonal Se crystallizes by constructing weakly coupled helix chains along the c-axis and eightfold rings, respectively [52] . The bonds in hexagonal Se are relatively stronger within helical chains along the hexagonal axis but weakly bonded between them.

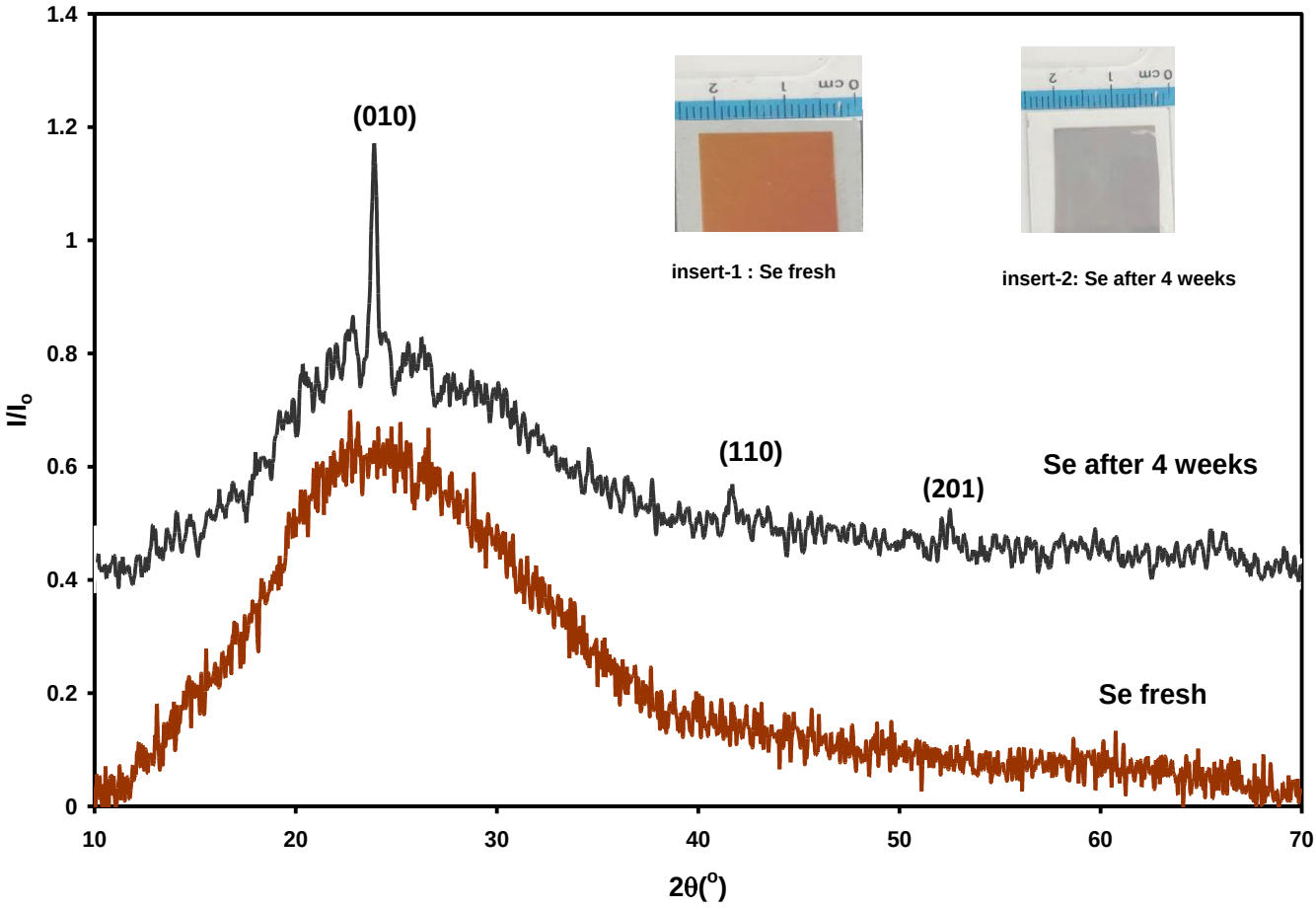

Fig. 4.1: The XRD patterns For Se fresh and Se after 4 weeks

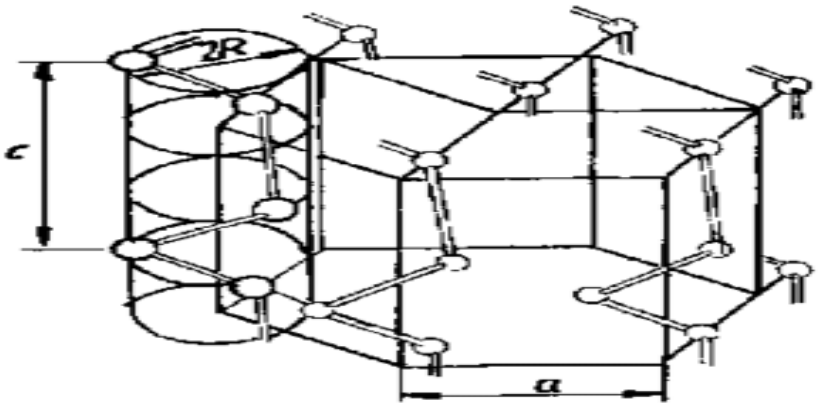

Fig.4.2: The Se hexagonal crystallize structure

4.1.2 Se/$CdBr_2$ Heterojunction:

The X-ray diffraction diffraction (XRD) patterns of Se, $CdBr_2$ and Se/$CdBr_2$ films after 4 weeks of preperation are presented in Fig.4.3.

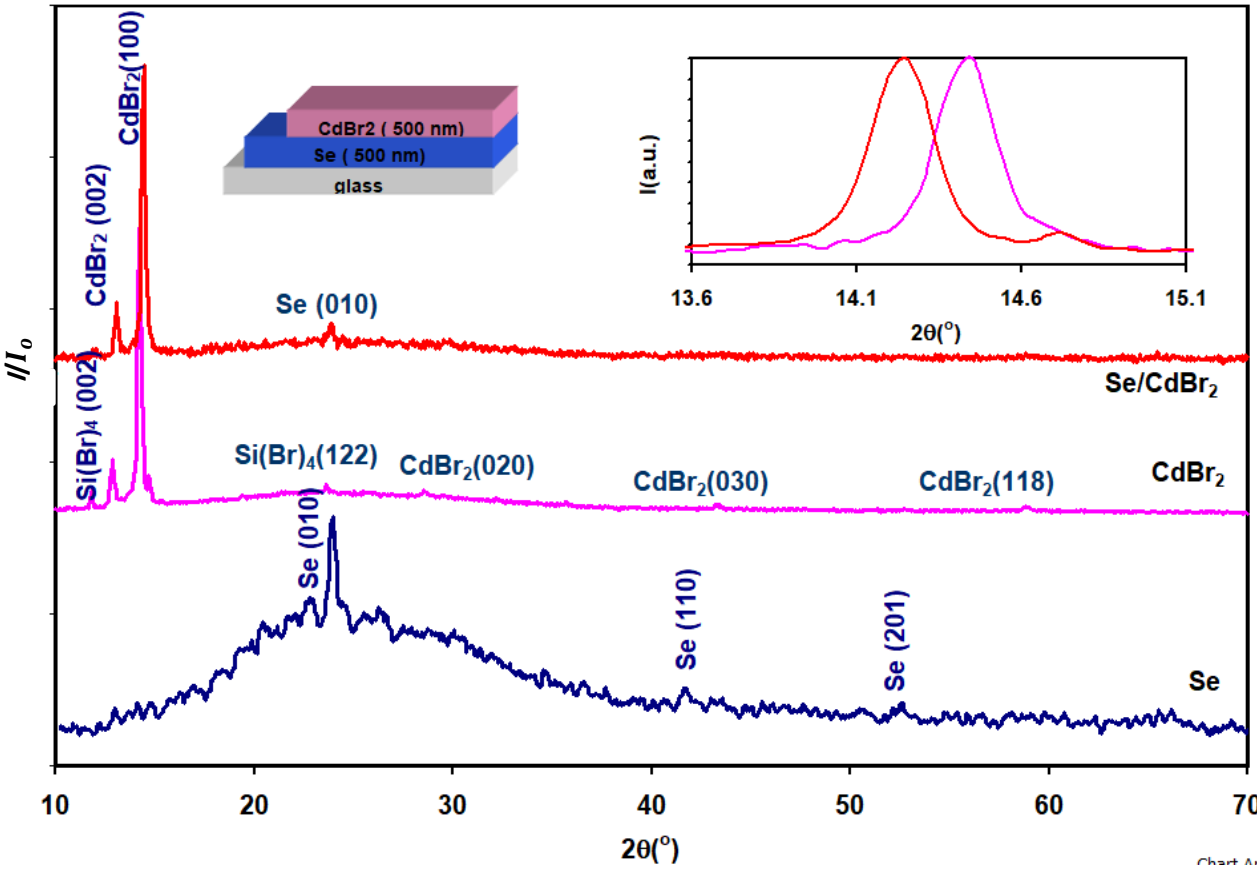

Fig. 4.3: The x-ray diffraction (XRD) patterns for Se, **$CdBr_2$** and Se/**$CdBr_2$** heterojunction devise, insert-1 shows the shift in XRD main peak.

The X-ray diffraction (XRD) patterns of Se, $CdBr_2$ and Se/$CdBr_2$ films are presented in fig.4.3. For Se films, as previously mentioned it shows three peaks. The most intensive peak was observed at diffraction angle $2\theta = 23.85^o$ and the two minor peaks are located at $2\theta = 41.55^o$and at $2\theta = 52.35^o$. On the other hand, the X-ray diffraction pattern of $CdBr_2$ films revealed seven peaks, with the most intensive peak appearing at a diffraction angle of $2\theta = 14.25^o$, $11.85^o, 12.76^o$, 23.75^o , 28.7^o , 59.1^o and 43.45^o.

Analysis of X-ray diffraction patterns angles was done by comparing the theoretically calculated ones with open crystallography data base (COD) and previous leterature data. The restriction for the acceptance of the structural phase was by assuming $\Delta\theta = \theta_{observed} - \theta_{calculation}$ being ≤ 0.2. For that to get the right structure indicated of $CdBr_2$ peaks by trying all possibilities can happen for the formation of the films. For example, the first expected structure comes from the interaction of cadmium with bromide so that, the second, third, fifth, sixth and seventh peaks match with the theoretical peaks of hexagonal $CdBr_2$ structure with apace group (P63mc) and lattice parameter (a = 7.17 Å, c = 13.87 Å and $\alpha = 90^o$, $\beta = 90^o$and $\gamma = 120^o$) [53]. Two peaks did not match any known structure of $CdBr_2$, the unknown peaks were at $2\theta = 11.85^o$ and 23.75^o. To find out the origin of these peaks, we assumed possible oxidation of $CdBr_2$ and unbounded Cd atoms may have formed CdO and CdOH. The expected diffraction patterns for these two minor phases were obtained by the "Crystdiff" software packages.

Another tested possibility was the interaction of bromine with Si in the $SiO_2: Na_2: MgO: CaO$ glass substrates. The possible phase is $SiBr_4$. $SiBr_4$ is a monoclinic structure of a space group (P21/c14) and lattice parameters (7.34 Å , 11.231 Å, 11.381 Å, 77.284^o, 90^o *and* 90^o)). It is evident from Fig.4.4 that the experimentally determined unknown peaks are assignable to $SiBr_4$.

Fig.4.4 also demonstrates the XRD patterns for Se/$CdBr_2$ interfaces. The XRD pattern of Se/$CdBr_2$ displayed four peaks. The position of the maximum peak that was assigned to $CdBr_2$ are shifted from 14.25^o to 14.45^o. In addition, the other peak position are also shifted from 11.25^o to 12.05^o, from 12.76^o to 13.05^o and from 23.75^o to 23.95^o. The strongest two peaks that represent the hexagonal phase of $CdBr_2$ films have (002) and (100) plane orientation direction structure, the first peak of monoclinic $SiBr_4$ being best oriented along the (002) direction. The peak located at a diffraction angle of $2\theta = 23.95^o$ represent the hexagonal phase of Se films being oriented in the (010) direction.

For further clarity of correlation between the theoretical estimated X– ray patterns and hexagonal Se, hexagonal $CdBr_2$ and monoclinic $SiBr_4$ and experimental results, the data is demonstrated in fig.4.4.

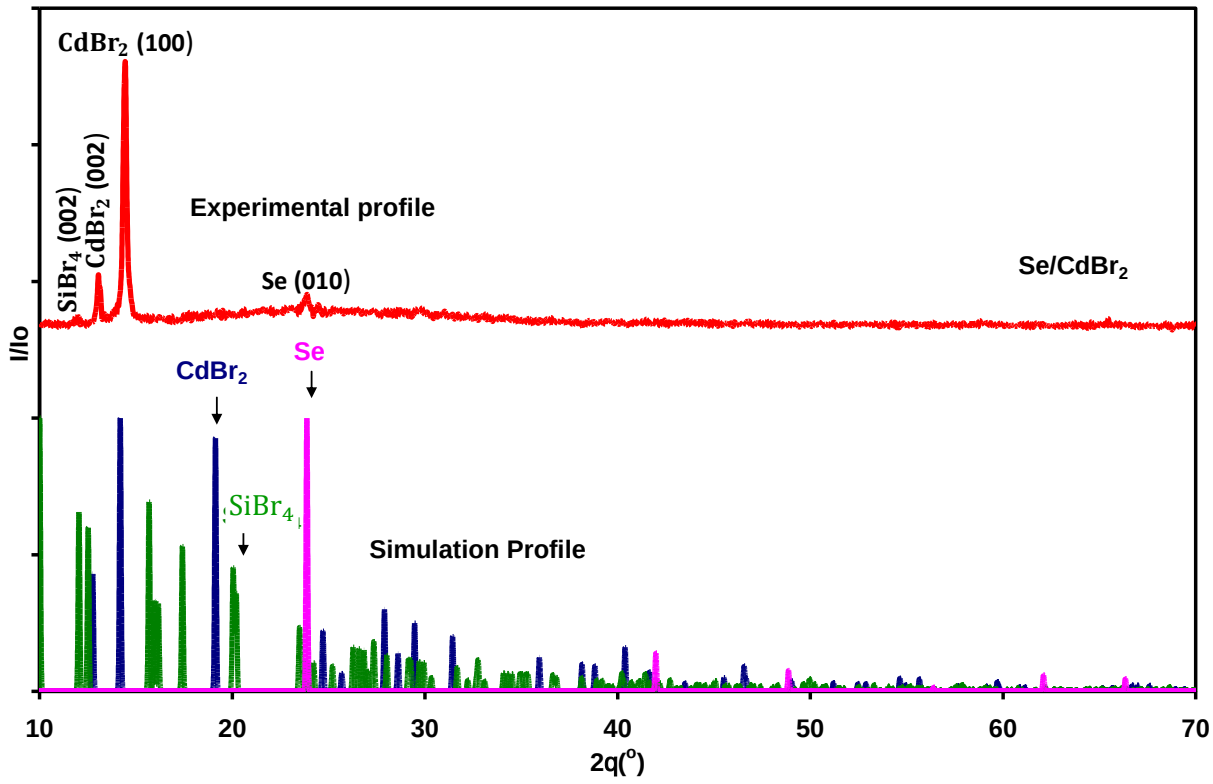

Fig. 4.4: The XRD patterns for Se/$\mathbf{CdBr_2}$ heterojunction, the green , pink and blue colored profile are estimated by "Crystdiff" software packages simulation for Se/$\mathbf{CdBr_2}$.

The effect of the deposition of $CdBr_2$ onto Se film on the major diffraction angle is shown in the inset of fig.4.3. It is shown in the inset of fig. 4.3 that the formation of Se/$CdBr_2$ caused a broadening and a lowering of the intensity of the major peak of Se. In particular, it decreases from 12391 to 1491 c/s and a right shift in peak position is clearly observed in the maximum peak. The peak located at $2\theta = 23.75^o$ shifted to $2\theta = 23.95^o$ that indicating the plastic deformation process [54].

The effect of deposition $CdBr_2$ onto Se films appears in the increase of the XRD intensity of the maximum peak from of 243 to 1491 c/s the data is shown in table 4.1. Analysis of reflection

peak of hexagonal Se/$CdBr_2$ heterojunctions result in an increase in the lattice constant values along the a and c-axis. The respective values are 12.26 Å and 7.83 Å, respectively.

The calculated crystallite size (D), micro strain (ε), defect density (δ) and stacking faults (SF) from the maximum peak of Se, $CdBr_2$ and Se/$CdBr_2$ are represented in table 4.1. These parameters are estimated using equ.2.8, equ 2.13, equ 2.14 and equ 2.15, respectively. Coating $CdBr_2$ onto Se increased the crystallite size of Se. In addition, coating $CdBr_2$ onto Se instead of glass increased the crystallite size of $CdBr_2$. The strain, stacking faults and defect density were also remarkably decreased. It is clear that coating on $CdBr_2$ onto Se enhances the structural properties of both materials.

Table 4.1 The structural parameteres of the main peak of Se , $CdBr_2$ and Se/$CdBr_2$ heterojunction device.

			Miller indices			Lattice constant (Å)					δ (X10^{12}line/cm^2)	
Sample	2θ (^{o})	I (a.u.)	h	K	L	a-axis	c-axis	D (nm)	$\varepsilon \times 10^{-3}$	SF %	a-axis	c-axis
Se	23.85	243	0	1	0	4.31	3.48	18	9.29	0.27	10.35	30.78
$CdBr_2$	14.25	12391	1	0	0	7.17	13.87	33	8.72	0.11	5.51	2.86
Se/$CdBr_2$	14.45	1491	0	1	0	7.08	13.56	41	6.88	0.09	2.04	3.20

4.2 Optical Analyses:

4.2.1 Optical Absorption in Se/$CdBr_2$

The optical transmittance (T%) and reflectance (R%) for Se (500 nm thick), $CdBr_2$ (500nm thick) and Se/$CdBr_2$ (1000nm thick) films are measured in incident light wave length (λ) range

190-1100 nm using evolution 350 spectrophotometer. The measured transmittance spectra for Se, $CdBr_2$ and Se/$CdBr_2$ heterojunctions are represented in fig.4.5. The fig.4.5 shows that Se film transmittance increased with increasing λ for $\lambda > 590$ nm (2.1eV), the heterojunction spectra more increase at 890 nm than single spectra, because of bonding process between selenium with bromide, which it close to infrared range. The transmittance spectra of Se displays two different transparency regions of 350-597 and 597-1083 nm. It is also clear from the fig. that the transmittance $CdBr_2$ is higher than that of Se and Se/$CdBr_2$. $CdBr_2$ films are highly transparent showing transmittance of 88 % at 370 nm.

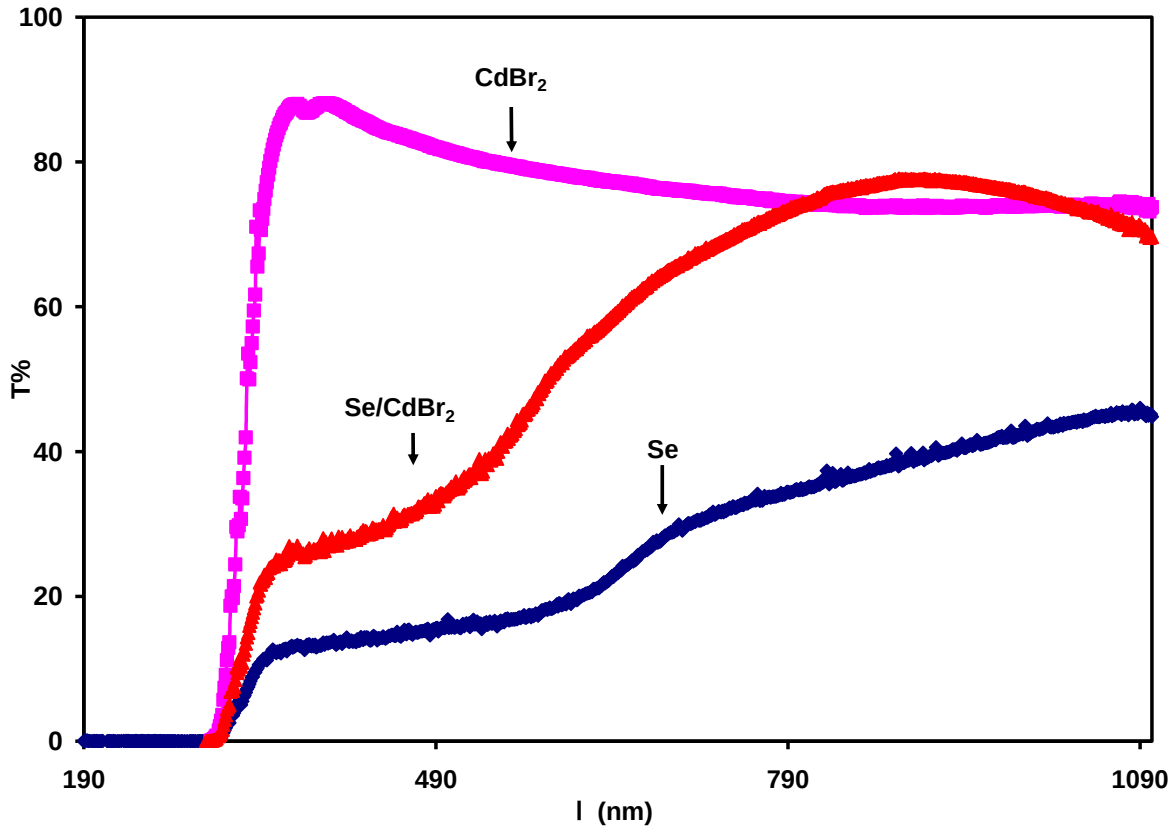

Fig. 4.5: Transmission spectra of Se, **$CdBr_2$** and Se/**$CdBr_2$** thin films

The optical reflectance spectra of Se, $CdBr_2$ and Se/$CdBr_2$ films are shown in Fig.4.6. As it is seen from the fig., the surface of $CdBr_2$ is more reflective than the surface of Se. The reflection Coefficient spectra of $CdBr_2$ displayed maximum peaks of 6.5% at λ = 278 nm. Then it decreases rapidly, reaching a minimum value of 1.7% at 353 nm. In the remaining region of Incident light increases with increasing $CdBr_2$. On the other hand, the deposition of $CdBr_2$ effect on reflectance of Se is evident from the increase in the number of the reflection interference patterns. Particularly, R% of Se/ $CdBr_2$ displays three maximum peaks of 7.2%, 9% and 11% at incident light wave length are 268, 392 and 681 nm, respectively. The interference patterns are assigned the constructive and destructive interference between light waves arriving at film's surface and those reflected at the bottom of the film [55] .

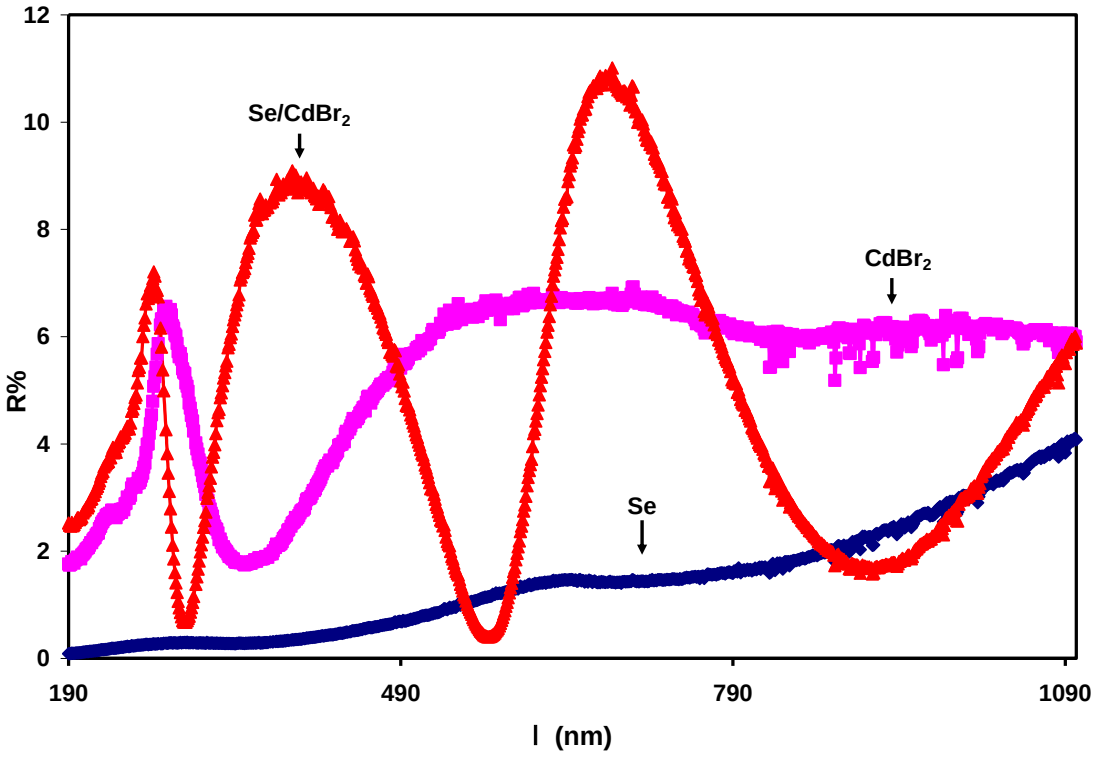

Fig. 4.6: Reflection spectra of Se, $\mathbf{CdBr_2}$ and Se/$\mathbf{CdBr_2}$ thin films.

The measured optical transmission and reflection coefficients are employed to determine the absorption coefficient (α) spectra for Se 0.5 μm(500 nm thick), $CdBr_2$ 0.5 μm (500 nm thick) and Se/$CdBr_2$ 1 μm (1000 nm thick). To get more information about the optical absorption of heterojunction α is calculated with the help of relation:

$$\alpha = -\frac{1}{d}\ln\left(\frac{T}{(1-R_g)(1-R_{g/Se})(1-R_{g/Se/CdBr_2})}\right) \qquad (4.117)$$

Where d is the film thickness. This equation is explained in the theoretical part of absorption multilayer thin films with incident photon energy. The relationship between the absorption coefficient (α) and the incident photon energy (E) is shown in fig.4.7.

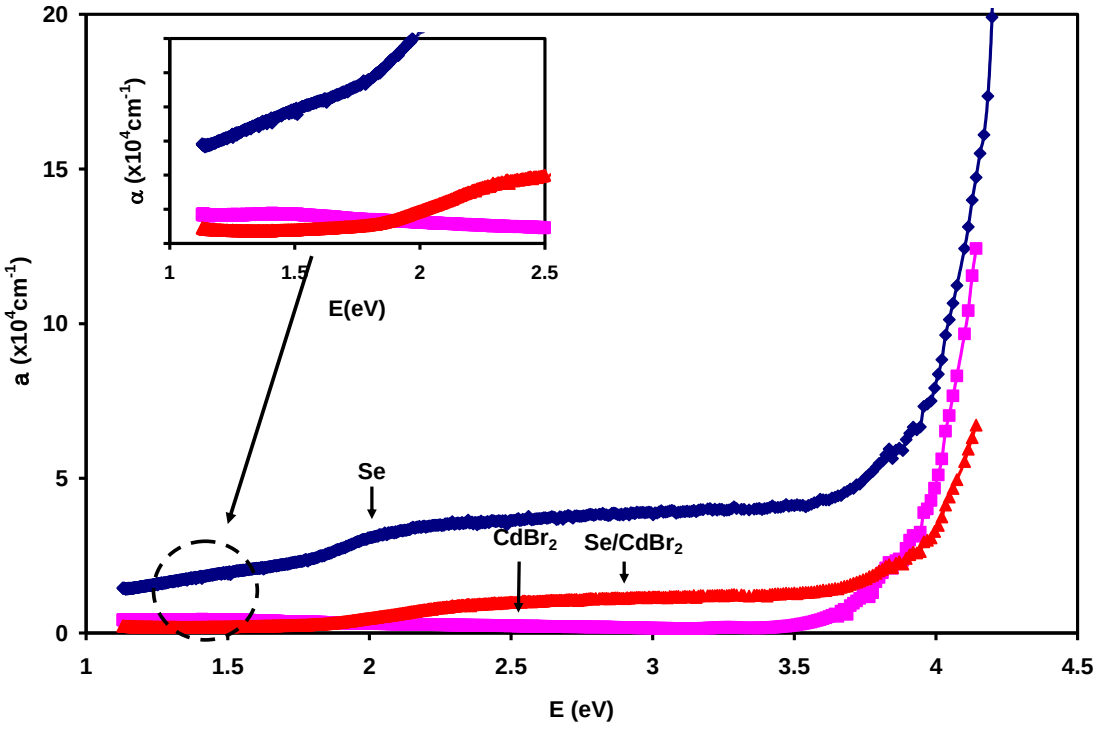

Fig. 4.7: The relation between absorption coefficient (α) and the incident photon energy in (eV) for Se, $\mathbf{CdBr_2}$ and Se/$\mathbf{CdBr_2}$ thin films.

As it readable from fig., the absorption coefficient spectra of Se, $CdBr_2$ and Se/$CdBr_2$ Films are observed to have two regions showing strong absorption in high energy range, between (2.00 – 4.00) eV and weak absorption in the low energy range at below 2.00 eV. The absorption coefficient for Se film exhibits higher absorption coefficient values compare $CdBr_2$ and Se/$CdBr_2$. It is also observed from the inset of Fig.4.7 that the α-spectra of Se films sharply decreases with decreasing photon energy, indicating that extended band tails may have existed in the band gap of Se. On the other hand, the weak absorption coefficient (α) in the region (1.48−2.00) eV. The absorption coefficient spectra of $CdBr_2$ showed an increase in the values of α with decreasing incident photon energy. This behavior assigned to the free carrier absorption

which is caused by dislocation, impurities and free electron and electron carrier transitions within conduction and valence band [56].

As a result, the absorption coefficient of the Se/$CdBr_2$ double layer in the weak absorption region shows a smoother decrease in α values with decreasing photon energy, probably due to the existence of band tails. Band tails appear due to the presence of defects [57]. Localized defects form band tails in the band gap region are hence responsible for the formation of absorption tails in α−spectra. As that the band tail associated with Urbach energy can be extracted from absorption spectra and calculated using the relation: $\alpha = \alpha_o e^{(E/E_o)}$, where E_o is Urbach energy. The Urbach energy (E_u) was calculated from the reciprocal slope of linear portion of Ln(α) versus photon energy plots as: $E_u = \frac{1}{slope}$, it was derivation equation for absorption coefficent to get: $ln\alpha = \frac{1}{E_u} E$. From the fig.4.8, that the band tail width E_u in Se and Se/$CdBr_2$ are 0.85 eV and 2.41 eV, respectively. The formation of these band tails is associated with orbital overlapping. The electronic configuration of Se, Cd and B are $4S^2 4P^4$, $4d^{10} 5S^2$ and $4S^2\ 4P^5$, respectively. Thus, band tails can be assigned to the orbitals overlapping of Br atoms with unfilled 4p orbits being overlapped with the 4P orbits of Se atoms.

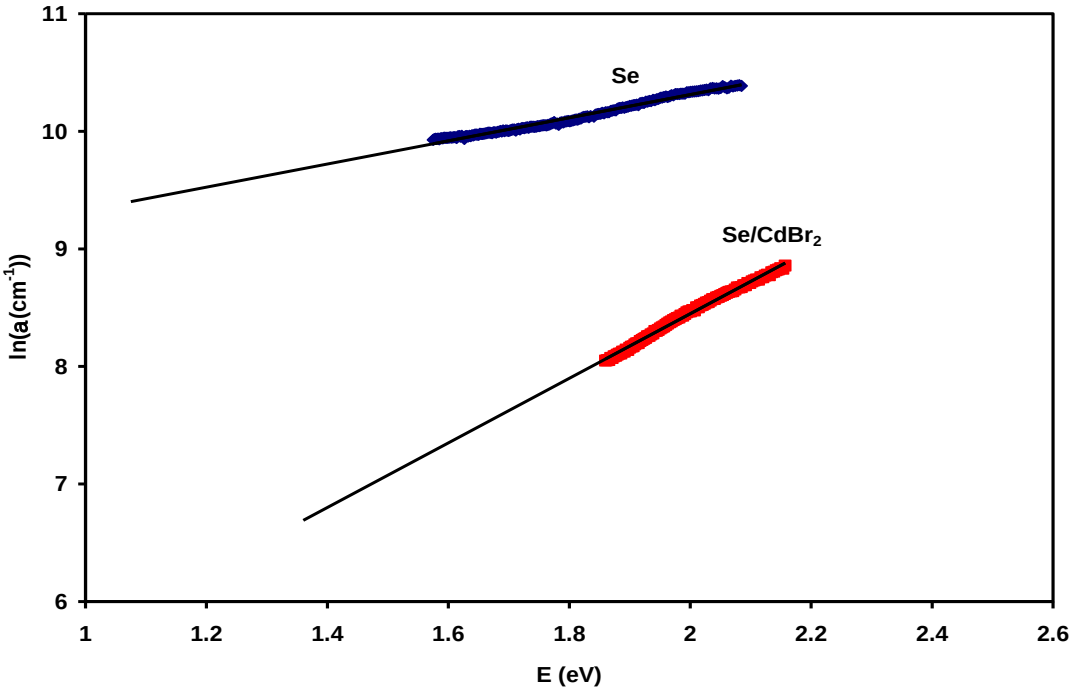

Fig. 4.8: The ln(α)-E variations for Se and Se/$CdBr_2$ heterojunction device.

In order to obtain more accurate information about the optical band gap of Se, CdBr2 single layers and Se/$CdBr_2$ heterojunction. The band gaps are calculated from the dependence of the absorption coefficient (α). On energy by applying Tauc's equation $(\alpha E)^P \alpha\,(E - E_g)$ was $(\alpha E)^P$ Vs photon energy plotted in the high and low absorption region of 1.0 - 4.5 eV for the mentioned films. The value of P indicates the types of band gap and has four value which an 2 for direct allowed, $\frac{1}{2}$ for indirect allowed, $\frac{1}{3}$ for indirect forbidden and $\frac{2}{3}$ for direct forbidden electronic transition. Computational tests have shown that for the $(\alpha E)^2$, $(\alpha E)^{\frac{1}{2}}$, $(\alpha E)^{\frac{1}{3}}$ and $(\alpha E)^{\frac{2}{3}} - E$ variation shown in Fig.4.9. The one that represent the band gap is the one which linear most of the experimental data.

As seen, the best fit data was obtained for $(\alpha E)^{\frac{1}{2}} - E$ indicating that the band gap is of an indirect allowed transition type for the Se, $CdBr_2$ and Se/$CdBr_2$. As fig. 4.10 (a) shows, the band gap in the high absorption region was calculated from the intercept solid straight line of the energy (E) – axis to denote indirect allowed transition energy.

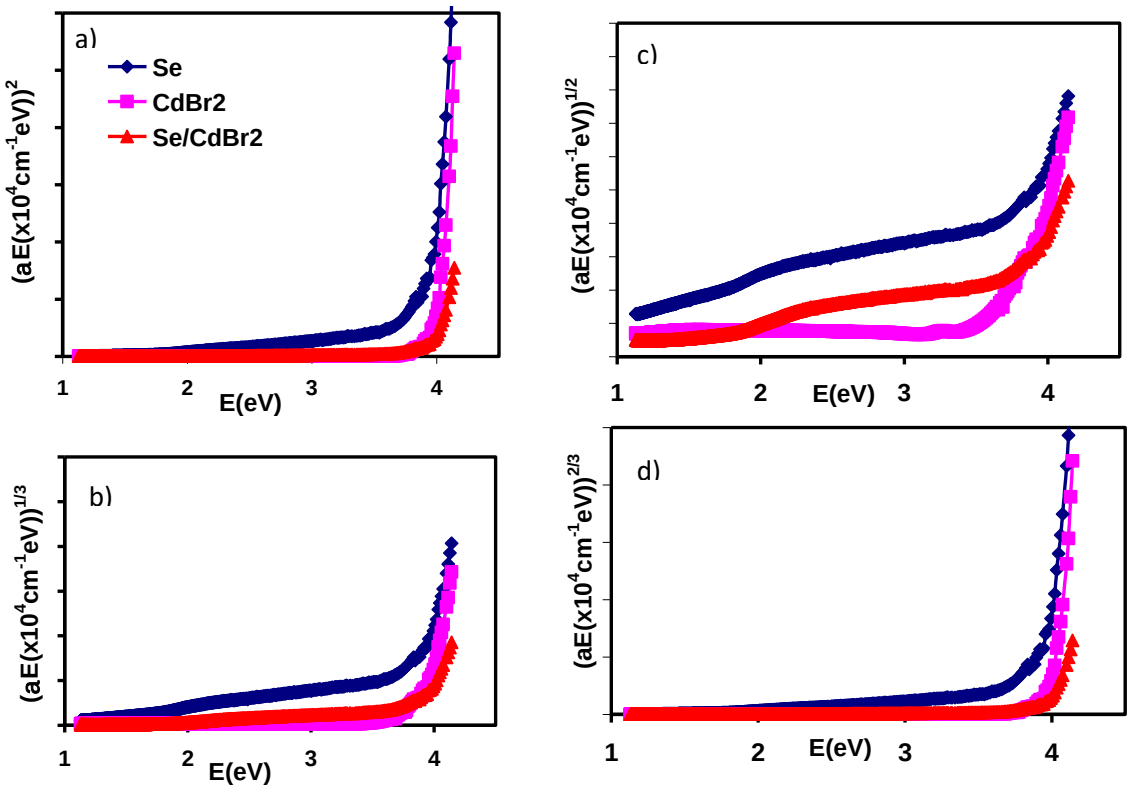

Fig. 4.9: $(\boldsymbol{\alpha E})^{\mathbf{2}}$, $(\boldsymbol{\alpha E})^{\frac{1}{2}}$, $(\boldsymbol{\alpha E})^{\frac{1}{3}}$ **and** $(\boldsymbol{\alpha E})^{\frac{2}{3}}$ -E variation of Se, $\mathbf{CdBr_2}$ and Se/$\mathbf{CdBr_2}$ measurement.

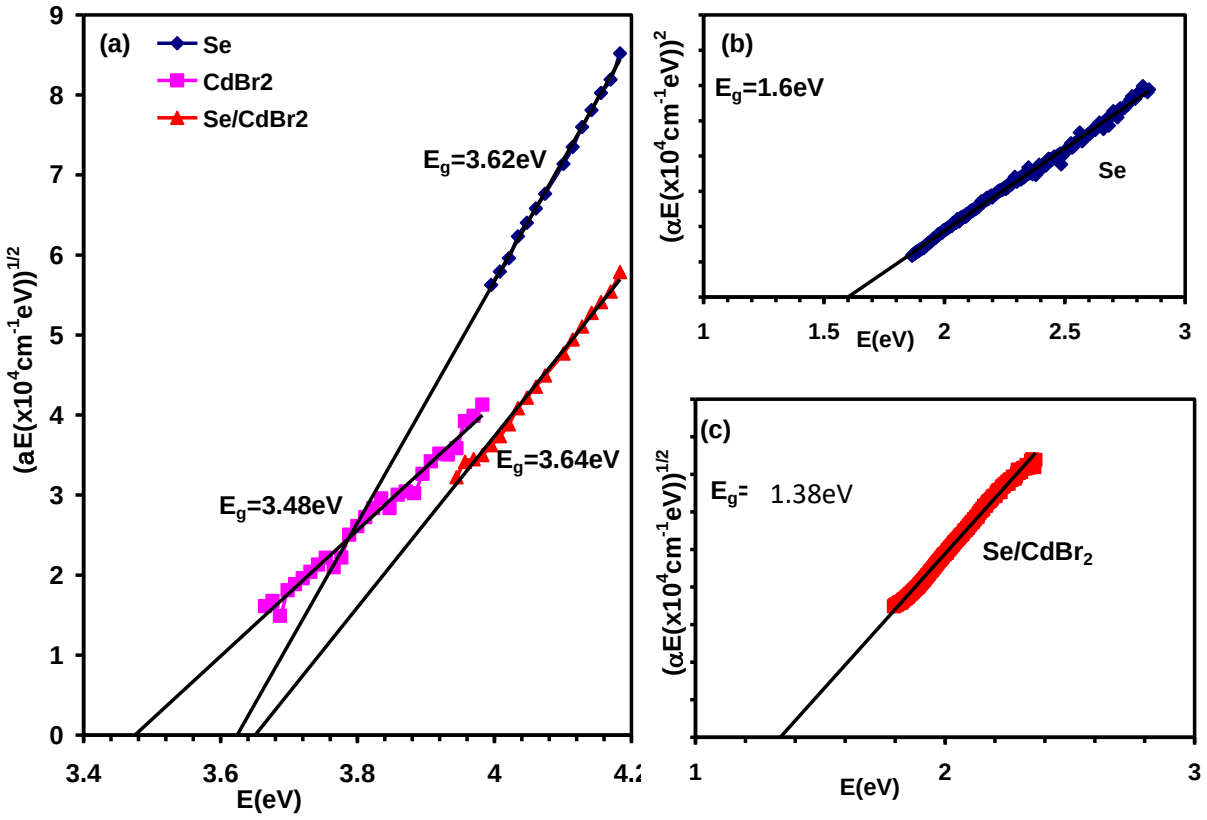

Fig. 4.10: (a) The $(\alpha E)^{1/2}$ Vs E for Se, $CdBr_2$ and Se/$CdBr_2$ heterojunction, (b) $(\alpha E)^{2}$ Vs E for Se and (c) $(\alpha E)^{1/2}$ Vs E for Se/$CdBr_2$

The band gap values, for Se of 3.62 eV as appearance from the plot, whereas for $CdBr_2$ being is 3.48 eV is comparable with 3.32 eV [58] reported for the hexagonal $CdBr_2$. In addition, the formation of Se/$CdBr_2$ hetrojunction bad gaps of 3.64 eV. Selenium thin films additionally display another energy band gap in the visible range of light if one plots $(\alpha E)^{2}$ Vs E in the low range of $(1.0-3.0)$ eV which should be found in a direct energy gap of 1.6 eV. For that is effect in the energy gap of Se/$CdBr_2$ double layers to found from plot (c) of $(\alpha E)^{1/2}$ Vs E in the low range of $(1.0-3.0)$ eV to become the second direct energy gap of 1.38 eV.

Recalling that the conduction band offset (ΔE_c) is the difference between the electron affinities of $CdBr_2$ and of Se, the respective affinities are 3.27 eV and 1.25 eV. Hence the valence band offset $\Delta E_v = (\Delta E_g - \Delta E_c)$ is (3.48-1.6-1.25) = 0.63 eV. The band offset are large enough to actualize quantum confinement in the films.

4.2.2 The Properties of The Dielectric Constant:

In order to accurately determine the application range of the Se, $CdBr_2$ single layer and Se/$CdBr_2$ heterojunction, we studied the dielectric properties of these films. The effective delectric constant ($\varepsilon_{eff} = \varepsilon_r + i\,\varepsilon_{im}$) and extinction coefficient ($k = \alpha\lambda/4\pi$) of the studied samples are calculated with the help of reflectance and absorption coefficient. The real part of the dielectric constant spectra for Se, $CdBr_2$ and Se/$CdBr_2$ are illustrated in fig.4.11. As shown, the ε_r spectra for Se films show an almost constant behavior which slowly increases with the decreasing incident photon energy until reaching 1.6 values at an incident photon energy of 1.9 eV between the ultraviolet and the visible regions, then it follows a sharper increase, exhibiting a maximum values of 2.25 at 1.13 eV for the infrared region.

The $CdBr_2$ spectrum shows decreasing dielectric constant values with decreasing incident photon energy in the ultraviolet region, showing a minimum value of 3.5 at 1.71 eV. One interesting behavior of these structures is that, the ε_r spectrum sharper increased display a broaden peak of $\varepsilon_r = 2.29$ at critical energy of 2.86 eV which can be assigned from the transition to the top of the valence band of $4p-$ state to the minimum conduction band at $1.25\,eV$ of bromine[59] . The deposition of $CdBr_2$ onto Se thin film, shows two resonance peaks of ε_r spectra; the first is very wide peak and extends From UV – region at 4.1 eV to visible light region region 2.1 eV with maxima peak value 3.16 eV. In addition, the second peak displayed a maximum of 4.0 eV

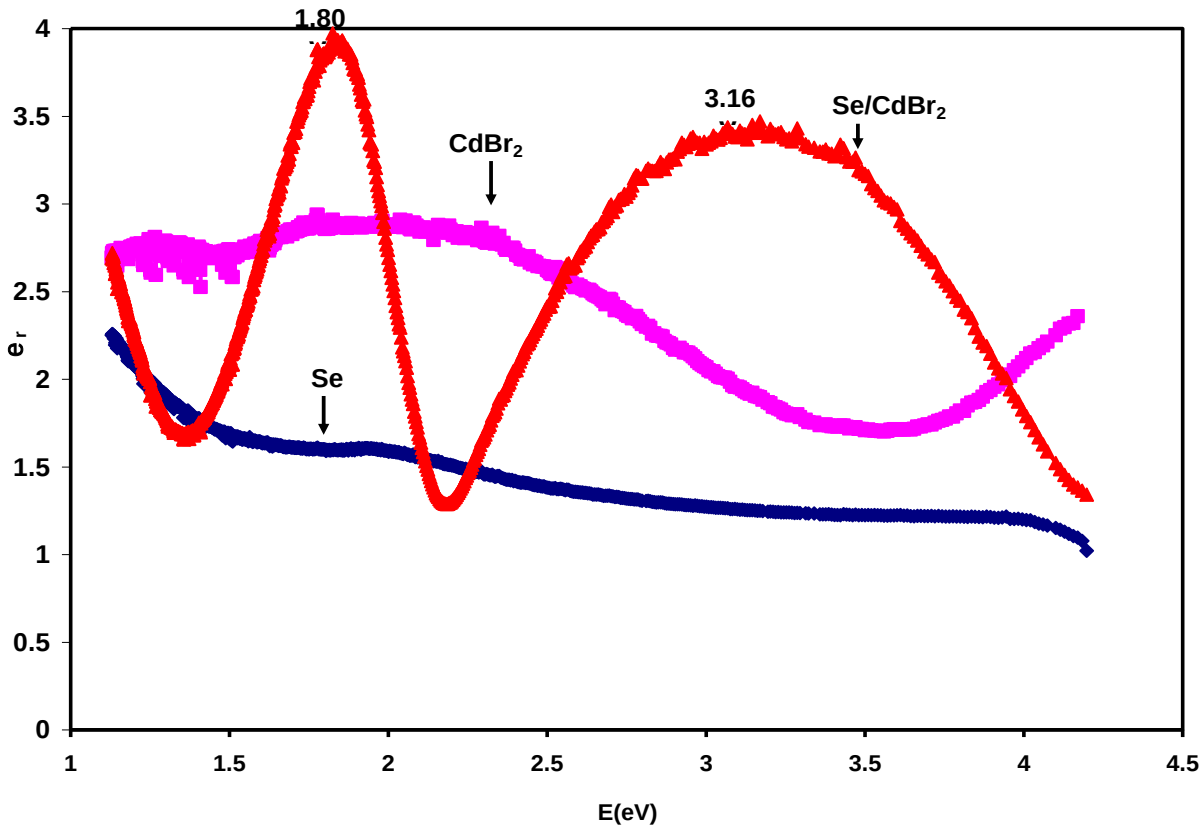

Fig. 4.11: The real part of the dielectric spectra for Se, $\mathbf{CdBr_2}$ and Se/$\mathbf{CdBr_2}$.

The peaks at critical energy values of 1.80 and 3.16 eV are assigned to the overlap of the Se with $CdBr_2$, so we can think of another way in which the peak at 1.80 eV is ascribed to the transition between the Cd-Se bonds [60]. In this process, the transition to 1.25 eV to 0.65 eV in the band gap of CdSe. While the peak located at 3.16 may be referred to interaction of the Se-$CdBr_2$ but no literature data is available about this transition. Mostly, the interaction between bromide nanoparticle, which it exactly assigned to transition between Br-Br bonds could account for this peak [61].

4.2.3 Imaginary Part:

The imaginary part of dielectric spectra ($\varepsilon_{\mathrm{im}}$) which are measured through using equation 2.83 Se, $CdBr_2$ single layers and Se/$CdBr_2$ double layers as shown in fig. 4.12. The spectra can be used to get information about the parameters of optical conductivity ($\sigma(\omega) = (\varepsilon_{\mathrm{im}}/4\pi), \omega$ is the angular frequency) , electron plasma interaction frequency (ω_p) and free electron mobility. In fig.4.12, the ε_{im} exhibits a lower value than the real part. In general, the imaginary part spectra of all films shows similar behavior. Namely, it starts to decrease sharply with decreasing incident light energy till reaching 4.0 eV value. Then, follow different trends. The ε_{im} spectra of Se shows a higher response than the other curves. While maintaining a similar behavior, it starts declining sharply reaching a value of 0.26 at 3.6 eV and then, increases slowly reaching the highest point at 0.39 at a 2.0 eV. In the lower range of incident photon energy ε_{im} remain constant displaying a value of 0.38 at 1.14 eV.

The imaginary part value of the $CdBr_2$ begins decreasing with decrease the incident photon energy, but in another behavior different as it reaches the lowest value at 3.4 eV. ε_{im} of $CdBr_2$ slowly increases until it reaches a value of 0.12 at 1.1 eV. More important feature of the spectra of Se coated with $CdBr_2$ shows a decrease until reaching value of 0.1at 3.6 eV and then remains constant in the energy range of 3.6 – 2.4 eV. As it is clear from the fig., it shows a small drop in the form of the bottom, where it takes a value of 0.1 at 2.1 eV and then shows for the depression reaching it's lowest point of 0.03 at 1.36 eV.

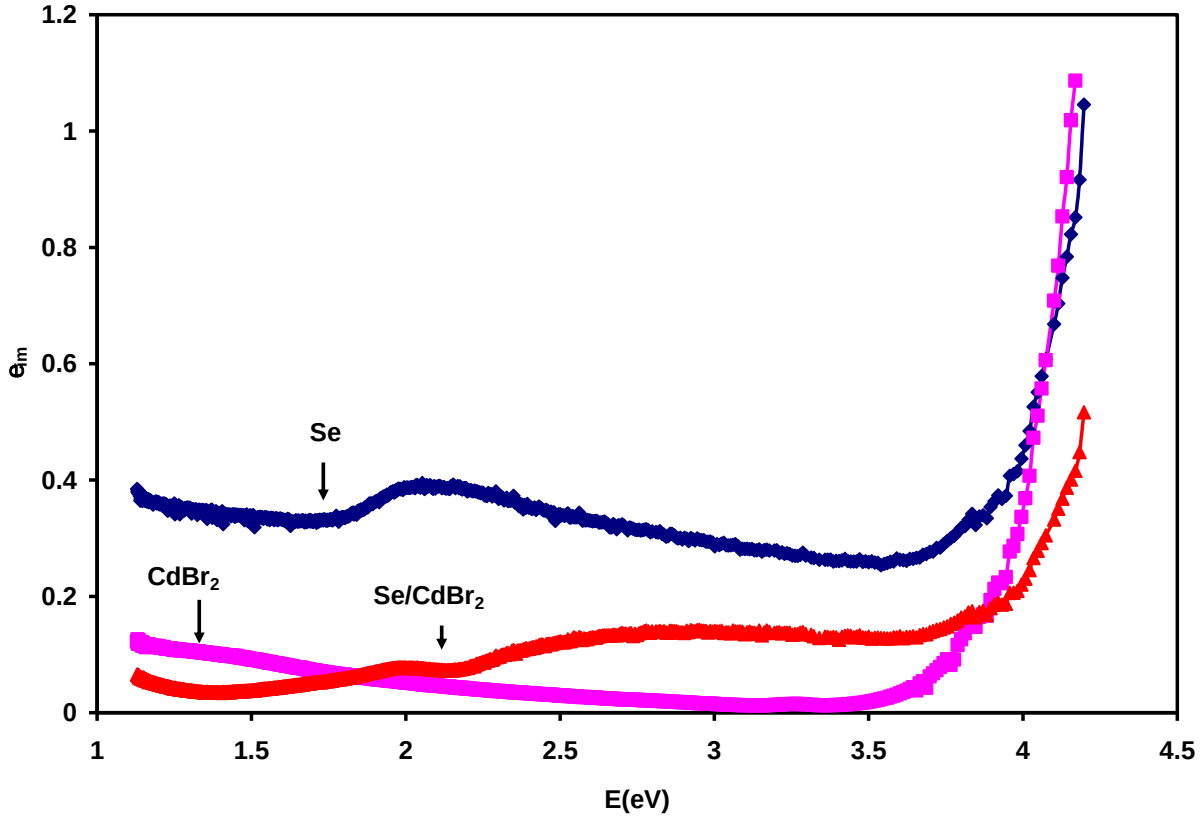

Fig. 4.12: The imaginary part of dielectric spectra ($\boldsymbol{\varepsilon_{im}}$) for Se, $\mathbf{CdBr_2}$, Se/$\mathbf{CdBr_2}$ heterojunction.

To reveal information about the effect of surface Plasmon interaction in Se, $CdBr_2$ and Se/$CdBr_2$ heterojunction, the imaginary part of dielectric constant spectra is modeled using the Drude – lorentz model through rewriting the equation:

$$\varepsilon_{im} = \sum_{i=1}^{i} \frac{w_{pei}^2 \, w}{((w_{ei}^2 - w^2)^2 + w^2 \, \tau_i^{-2})} \qquad (4.118)$$

Where k is the number of dominate linear oscillators, $w_{pe} = \sqrt{4\pi p e^2/m^*}$ is the hole bounded Plasmon frequency, $w = 2\pi f$ is the angular frequency of the incident light, w_e is the reduced resonant frequency, τ is the average scattering time and represents the inverse of the damping

coefficient. m^* is the free carrier effective mass and p is the free hole density. In addition, the free-carriers mobility can be measured by the rule of $\mu = e\tau/m^*$.

Using the effective mass of Se, $CdBr_2$ and $Se/CdBr_2$, the experimental data were reproduced by fitting equation of 4.118 through substituting the value of p-Se m_{Se}^* is 0.35 m_o and the p-$CdBr_2$ $m_{CdBr_2}^*$ is 0.45 m_o, the reduced mass of $Se/CdBr_2$ heterojnction was evaluated from the relation $m^*{}_{Se/CdBr2} = ((m^*{}_{Se})^{-1} + (m^*{}_{CdBr2})^{-1})^{-1} = 0.12\ m_0$. In Fig.4.12. Displays the theoretical fitting plots of ε_{im} spectra of (a) Se, (b) $CdBr_2$ and (c) $Se/CdBr_2$. Assuming the presence of four oscillators, i = 4 was sufficient to reproduce the $\sigma(w)$ data, which is shown by a black colored curve as it describes the theoretical fitting data of ε_{im} spectra.

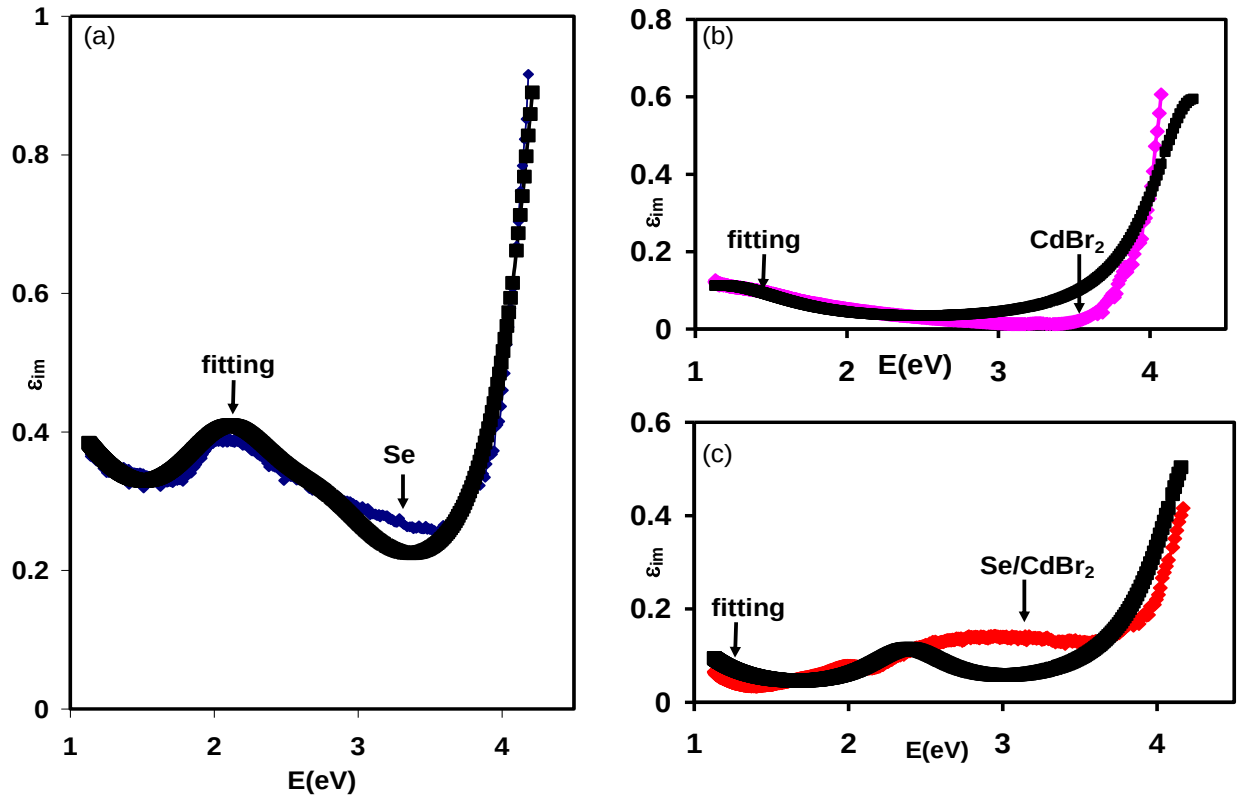

Fig. 4.13: The imaginary part of the dielectric spectra for (a) Se, (b) **$CdBr_2$** and (c) Se/**$CdBr_2$** heterojunction. The black colored plots represent the fitting which is achieved by Eqn.4.118

Fig.4.13 indicates the correlation between the theoretical and experimental spectra. The good correlation between the experimentally found and theoretically calculated is obtained by substituting the values shown in Table 4.2.

Table 4.2 (a) the optical conduction parameter for hole-Plasmon interaction of se film.

.. *i*	1	2	3	4
τ (*f*s)	0.4	0.6	0.6	1.0
P (x10^{17} cm^{-3})	120.0	120.0	80.0	670.0
W_e (x10^{15} Rad/s)	1.5	3.3	4.3	6.7
E_e (eV)	0.98	2.16	2.82	4.40
W_p (GHz)	3.48	3.48	2.84	8.22
μ (cm^2/Vs)	2.01	3.01	3.01	5.02

Table 4.2(b) the optical conduction parameter for electron-Plasmon interaction of $cdBr_2$ film.

i	1	2	3	4
τ (*f*s)	0.4	0.6	1.0	1.0
P (x10^{17} cm^{-3})	10.0	32.0	400.0	70.0
W_e (x10^{15} Rad/s)	1.5	2.0	6.5	7.0
E_e (eV)	0.98	1.31	4.26	4.59
W_p (GHz)	0.89	1.59	5.60	2.34
μ (cm^2/Vs)	1.56	2.34	3.91	3.91

Table 4.2(c) the optical conduction parameter for electron-Plasmon interaction of se/$CdBr_2$ film.

i	1	2	3	4
τ (*f*s)	1.0	1.0	1.0	1.0
P (x10^{17} cm^{-3})	10.0	10.0	50.0	60.0
W_e (x10^{15} Rad/s)	1.0	3.7	6.5	6.5
E_e (eV)	0.66	2.39	4.26	4.26
W_p (GHz)	1.72	1.72	3.84	4.20
μ (cm^2/Vs)	14.65	14.65	14.65	14.65

As can be seen from the tables, the observed result of the best fitting parameters of the experimental curve, which involved the value of the hole scattering time (τ), reduced resonant frequency (w_e), the drift mobility (μ) and the electron bounded plasma frequency (w_P). The hole scattering time increased from 0.4 to 1.0 *f*s when deposited the $CdBr_2$ onto Se. The reduced resonant frequency of Se was 1.50×10^{15} Rad/s and decrease to 1.0×10^{15} Rad/s when $CdBr_2$ added to the Se, with taken into account, for these state the reduced resonant value of $CdBr_2$ is the same about 1.50×10^{15} Rad/s. In addition, the free hole density P for Se, $CdBr_2$ and Se/$CdBr_2$ are found to be 120, 10 and $10 \times 10^{17} cm^{-3}$, respectively. Moreover, the drift mobility, which shows a value of $2.01 cm^2/Vs$ for Se to a higher increase of the Se/$CdBr_2$ of 14.65 cm^2/Vs. Finally, the plasma frequency (w_p) for Se decreases upon deposition of $CdBr_2$ from 3.48 to 1.72 GHz. Although coating of $CdBr_2$ onto Se decreased the maximum achievable plasmon frequency of Se 8.22 GHz to 4.2 GHz, it remarkably enhanced, the drift mobility valence. The charged particles become more effective in the presence of $CdBr_2$.

Chapter Five

Conclusions

In this thesis, we have shown the possible formation of a new class of optical interfaces that can be employed as dielectric resonators suitable for near infrared and visible light dielectric band applications. The optical interfaces are formed by physically stacking $CdBr_2$ onto Se thin films using thermal evaporation techniques. Various methods, including X-ray diffraction, scanning electron microscopy and optical spectrophotometry, were employed to explore the physical nature of the proposed interfaces: The two stacked layers are found to form from hexagonal mismatched structures causing valence and conduction band offsets of $1.25\,eV$ – 0.65 eV respectively. The stacked layer, showed a narrower energy band gap of Se. The dielectric dispersion in the films showed well defined dielectric near 3.1 eV and 1.8 eV. The optical interfaces displayed drift mobility values of 14 cm^2/vs which is 12 times larger than that of Se or $CdBr_2$. The enhanced drift mobility, which is accompanied by Plasmon frequency in the gigahertz frequency domain, makes the Se/$CdBr_2$ interface ideal for optical communication technology.

References:

[1] Yoo, H., Kim, W.-G., Kang, B. H., Kim, H. T., Park, J. W., Choi, D. H., … Kim, H. J. (2020). High photosensitive Indium–Gallium–Zinc Oxide Thin-Film Phototransistor with a Selenium Capping Layer for Visible Light Detection. ACS Applied Materials & Interfaces.

[2] Wang, Y., Zhao, Y., Ding, X., & Qiao, L. (2021). Recent advances in the electrochemistry of layered post-transition metal chalcogenide nanomaterials for hydrogen evolution reaction. Journal of Energy Chemistry, 60, 451-479.

[3] Huang, Y., Su, E., Ren, J., & Qu, X. (2021). The recent biological applications of selenium-based nanomaterials. Nano Today, 38, 101205.

[4] BAE, Minkyung; KIM, Hyeyoung. The role of vitamin C, vitamin D, and selenium in immune system against COVID-19. Molecules, 2020, 25.22: 5346.

[5] Qin, JIngkai; Zhou, Feichi; Wang, Jingli; Chen, Jiewei; Wang, Cong; Guo, Xuyun; Zhao, Shouxin; Pei, Yi; Zhen, Liang; Ye, Peide D.; LAU, Shu Ping, Zhu, Ye; Xu, Cheng-Yan; Chai, Yang (2020). Anisotropic Signal Processing with Trigonal Selenium Nanosheet Synaptic Transistors. ACS Nano, (), acsnano.0c03124

[6] Sharad Pandey, Rashmi Chauhan, Optical and structural modification in amorphous Ge24Se61Sb15 thin films under 80 MeV Silicon swift heavy ions for telecom and optical applications, Optical Materials, Volume 1112021, 110686, ISSN 0925-3467

[7] Gibson, U. J., Wei, L., & Ballato, J. (2021). Semiconductor core fibres: materials science in a bottle. Nature Communications, 12(1), 1-15.

[8] Youngman, T. H., Nielsen, R., Crovetto, A., Seger, B., Hansen, O., Chorkendorff, I., & Vesborg, P. C. K. (2021). Semitransparent Selenium Solar Cells as a Top Cell for Tandem Photovoltaics. Solar RRL, 5(7), 2100111.

[9] Gupta, G. K., & Dixit, A. (2018). Theoretical studies of single and tandem Cu2ZnSn (S/Se) 4 junction solar cells for enhanced efficiency. Optical Materials, 82, 11-20.

[10] Foody, M. J., Weimer, M. S., Bhandari, H., & Hock, A. S. (2021). Comparison of Ligand Architecture on Vapor Deposition Precursors: Synthesis, Characterization, and Reactivity of Volatile Cadmium Bis-Amidinate Complexes. Inorganic Chemistry, 60(9), 6191–6200.

[11] Wang, Fei; Jia, Lemin; Ding, Ying; Cai, Haihuai; Zheng, Wei; Huang, Feng (2020). Ultraâ€ • Long Van Der Waals CdBr2 Micro/Nanobelts. Small Methods, (), 2000501–.

[12] Malgras, V., Ji, Q., Kamachi, Y., Mori, T., Shieh, F. K., Wu, K. C. W., ... & Yamauchi, Y. (2015). Templated synthesis for nanoarchitectured porous materials. Bulletin of the Chemical Society of Japan, 88(9), 1171-1200.

[13] Qasrawi, A. F., & Hamarsheh, A. A. (2021). Design of Au/Cdbr 2/Au as Negative Capacitance Devices and as Band Filters Suitable for 4G Technologies. Materials Research, 24.

[14] Nishimura, H., Enomoto, K., Pu, Y. J., & Kim, D. (2022). Hydrothermal synthesis of water-soluble Mn-and Cu-doped CdSe quantum dots with multi-shell structures and their photoluminescence properties. RSC advances, 12(10), 6255-6264.

[15] Zou, S., Yang, G., Pang, T., Zou, M., Liu, R., Chen, B., ... & Zou, B. (2018). One-step synthesis of nail-like Mn-doped CdS/CdBr2 hetero-nanostructures for potential lasing application. Nanotechnology, 30(7), 075605.

[16] Bertin, E. P. (2012). Principles and practice of X-ray spectrometric analysis. Springer Science & Business Media.

[17] Dolabella, S., Borzì, A., Dommann, A., & Neels, A. (2021). Lattice Strain and Defects Analysis in Nanostructured Semiconductor Materials and Devices by High-Resolution X-Ray Diffraction: Theoretical and Practical Aspects. Small Methods, 2100932.

[18] Fitzpatrick, M. E., Fry, A. T., Holdway, P., Kandil, F. A., Shackleton, J., & Suominen, L. (2005). Determination of residual stresses by X-ray diffraction.

[19] Ladd, Mark; Palmer, Rex (2013). Structure Determination by X-ray Crystallography

[20] Fatimah, S., Ragadhita, R., Al Husaeni, D. F., & Nandiyanto, A. B. D. How to calculate crystallite size from x-ray diffraction (XRD) using Scherrer method. ASEAN Journal of Science and Engneering, 2(1), 65-76.

[21] Cantelar, E., Sanz-García, J. A., Sanz-Martin, A., Santiuste, J. E. M., & Cussó, F. (2020). Structural, photoluminescent properties and Judd-Ofelt analysis of Eu3+-activated CaF2 nanocubes. Journal of Alloys and Compounds, 813, 152194.

[22] Elmorsi, T. M., Elsayed, M. H., & Bakr, M. F. (2017). Enhancing the removal of methylene blue by modified ZnO nanoparticles: kinetics and equilibrium studies. Canadian Journal of Chemistry, 95(5), 590-600.

[23] Qasrawi, A. F., & Omareya, O. A. (2019). In situ observations of the permanent structural modifications, phase transformations and band gap narrowing upon heating of Cu2Se/Yb/Cu2Se films. Journal of Alloys and Compounds, 785, 1160-1165.

.

[24] Sen, S. K., Barman, U. C., Manir, M. S., Mondal, P., Dutta, S., Paul, M., ... & Hakim, M. A. (2020). X-ray peak profile analysis of pure and Dy-doped α-MoO3 nanobelts using Debye-Scherrer, Williamson-Hall and Halder-Wagner methods. Advances in Natural Sciences: Nanoscience and Nanotechnology, 11(2), 025004.

[25] Tutantsev, A. S., Marchenko, E. I., Udalova, N. N., Fateev, S. A., Goodilin, E. A., & Tarasov, A. B. (2021). Structural Disorder in Layered Hybrid Halide Perovskites: Types of Stacking Faults, Influence on Optical Properties and Their Suppression by Crystallization Engineering. Nanomaterials, 11(12), 3333.

[26] Gamler, J. T., Leonardi, A., Sang, X., Koczkur, K. M., Unocic, R. R., Engel, M., & Skrabalak, S. E. (2020). Effect of lattice mismatch and shell thickness on strain in core@ shell nanocrystals. Nanoscale Advances, 2(3), 1105-1114.

[27] Bengtsson, Å. (2022). Time-Resolved X-ray Diffraction Studies of Laser-Induced Dynamics in Solids (Doctoral dissertation, Lund University).

[28] Wood III, A. C., & Qin, L. C. (2021). An Analysis of the Rhombohedral and Hexagonal Structures in Graphite.

[29] Viter, R., & Iatsunskyi, I. (2018). Optical spectroscopy for characterization of metal oxide nanofibers. Handbook of Nanofibers, 5, 1-35

[30] Sreekala, P. S., John, H., & Aanandan, C. K. (2020). Studies on anomalous dispersion behavior of PANI–CNT composites for enhanced shielding effectiveness in various microwave bands. Applied Physics A, 126(5), 1-14.

[31] Viter, R., & Iatsunskyi, I. (2018). Optical spectroscopy for characterization of metal oxide nanofibers. Handbook of Nanofibers, 5, 1-35.

[32] Zhang, W. D. (2020). Insights into the Planck Constant, the Conservation of Angular Momentum and the Property of Photons.

[33] Fox, M. (2002). Optical properties of solids.

[34]Sun, G. (2011). Intersubband approach to silicon based lasers—circumventing the indirect bandgap limitation. Advances in Optics and Photonics, 3(1), 53-87.

[35] Qasrawi, A. F., & Aloushi, H. D. (2019). In Situ Observation of Heat-Assisted Hexagonal-Orthorhombic Phase Transitions in Se/Ag/Se Sandwiched Structures and Their Effects on Optical Properties. Journal of Electronic Materials, 48(12), 7906-7914.

[36] Dresselhaus, M. S. (2001). Solid state physics part ii optical properties of solids. Lecture Notes (Massachusetts Institute of Technology, Cambridge, MA), 17, 15-16.

[37] Pankove, J. I. (2012). Optical processes in semiconductors. Courier Corporation.

[38] Akl, A. A., & Mahmoud, S. A. (2018). Effect of growth temperatures on the surface morphology, optical analysis, dielectric constants, electric susceptibility, Urbach and bandgap energy of sprayed NiO thin films. Optik, 172, 783-793.

[39] Dylla, M. T., Dunn, A., Anand, S., Jain, A., & Snyder, G. J. (2020). Machine learning chemical guidelines for engineering electronic structures in half-heusler thermoelectric materials. Research, 2020.

[40] Heiba, Z. K., Mohamed, M. B., Ahmed, S. I., & Alhazime, A. A. (2021). Tailoring the optical properties of PVA/PVP blend by doping with Cu/MnS nanoparticles. Journal of Vinyl and Additive Technology, 27(2), 410-418.

[41] Titov, S. V., Dowling, W. J., Kalmykov, Y. P., & Cherkasskii, M. (2022). Nutation spin waves in ferromagnets. Physical Review B, 105(21), 214414.

[42] Hao, J., Zhou, L., & Qiu, M. (2011). Nearly total absorption of light and heat generation by plasmonic metamaterials. Physical review B, 83(16), 165107.

[43] Kumar, A., Shukla, R. K., Kumar, A., & Gupta, R. (2019). Light induced effects & defects in chalcogenide glassy semicoductors: A review. Infrared Physics & Technology, 102, 103056.

[44] Pang, W. (2019). Optically Reconfigurable Microwave and Millimetre Wave Switches (Doctoral dissertation, University of Bristol).

[45] Marple, M., Badger, J., Hung, I., Gan, Z., Kovnir, K., & Sen, S. (2017). Structure of amorphous selenium by 2D 77Se NMR spectroscopy: an end to the dilemma of chain versus ring. Angewandte Chemie International Edition, 56(33), 9777-9781.

[46] Kalikka, J., Konstantinou, K., Akola, J., & Jones, R. O. (2021). Melt-quenched and as-deposited structures of amorphous selenium: a density functional/molecular dynamics comparison. Journal of Physics: Condensed Matter, 33(44), 445401.

[47] Koch, C., Hansen, A. L., Dankwort, T., Schienke, G., Paulsen, M., Meyer, D., ... & Bensch, W. (2017). Enhanced temperature stability and exceptionally high electrical contrast of selenium substituted Ge 2 Sb 2 Te 5 phase change materials. Rsc Advances, 7(28), 17164-17172.

[48] Liu, H., Wang, L., Xiao, X., De Carlo, F., Feng, J., Mao, H. K., & Hemley, R. J. (2008). Anomalous high-pressure behavior of amorphous selenium from synchrotron x-ray diffraction and microtomography. Proceedings of the National Academy of Sciences, 105(36), 13229-13234.

[49] Saleh, M. H., Jafar, M. M. A. G., Bulos, B. N., & Al-Daraghmeh, T. M. (2014). Determination of optical properties of undoped amorphous selenium (a-Se) films by dielectric modeling of their normal-incidence transmittance spectra. Applied Physics Research, 6(6), 10.

[50] Shi, C., Luo, X., Qi, P., Li, T., Song, S., Najdovski, Z., ... & Ren, H. (2016). Shape sensing techniques for continuum robots in minimally invasive surgery: A survey. IEEE Transactions on Biomedical Engineering, 64(8), 1665-1678.

[51] Levin, E. E., Kitchaev, D. A., Eggeler, Y. M., Mayer, J. A., Behera, P., Gianola, D. S., ... & Seshadri, R. (2021). Influence of plastic deformation on the magnetic properties of Heusler MnAu 2 Al. Physical Review Materials, 5(1), 014408.

[52] Liu, W., Lustig, W. P., & Li, J. (2019). Luminescent inorganic-organic hybrid semiconductor materials for energy-saving lighting applications. EnergyChem, 1(2), 100008.

[53] Qasrawi, A. F., & Hamarsheh, A. A. (2021). Band offsets, electron affinities and optical dynamics at the CdBr2/SiO2 interfaces. Optik, 243, 167467.

[54] Qasrawi, A. F., & Zyoud, H. M. (2020). Optical Dynamics at the Au/ZnPc Interfaces. Materials Research, 23.

[55] Cotton, D. E., & Roberts, S. T. (2021). Sensitivity of sum frequency generation experimental conditions to thin film interference effects. The Journal of Chemical Physics, 154(11), 114704.

[56] Liu, H. Q., & Yao, C. B. (2022). Composition engineering of AZO films for controlled photon–electron conversion and ultrafast nonlinear optical behavior. Nanoscale, 14(25), 9169-9191.

[57] Pan, L., Liu, Y., Yao, L., Ren, D., Sivula, K., Grätzel, M., & Hagfeldt, A. (2020). Cu2O photocathodes with band-tail states assisted hole transport for standalone solar water splitting. Nature communications, 11(1), 1-10.

[58] Qasrawi, A. F., & Hamarsheh, A. A. (2021). Band offsets, electron affinities and optical dynamics at the CdBr2/SiO2 interfaces. Optik, 243, 167467.

[59] Martín-Fuentes, C., Urgel, J. I., Edalatmanesh, S., Rodríguez-Sánchez, E., Santos, J., Mutombo, P., ... & Écija, D. (2021). Cumulene-like bridged indeno [1, 2-b] fluorene π-conjugated polymers synthesized on metal surfaces. Chemical Communications, 57(61), 7545-7548.

[60] Simi, N. J., Vinayakan, R., & Ison, V. V. (2019). Photoinduced electron transfer in novel CdSe–Cu 2 Se type II core–shell quantum dots. RSC advances, 9(26), 15092-15098.

[61] Fateev, S. A., Petrov, A. A., Marchenko, E. I., Zubavichus, Y. V., Khrustalev, V. N., Petrov, A. V., ... & Tarasov, A. B. (2021). FA2PbBr4: synthesis, structure, and unusual optical properties of two polymorphs of formamidinium-based layered (110) hybrid perovskite. Chemistry of Materials, 33(5), 1900-1907.

الملخص

الديناميكا الضوئية في واجهات $Se/CdBr_2$

في العمل الحالي ، قمنا بتصميم وتمييز فئة جديدة من أجهزة الاستقبال الضوئية. يتم تصنيع الواجهات الضوئية عن طريق ترسيب البخار الفيزيائي لـ $CdBr_2$ على ركائز السيلينيوم. تمت دراسة الخواص التركيبية والبصرية والعازلة للكهرباء لأغشية $Se/CdBr_2$ بالتفصيل. لوحظ أن الأغشية الرقيقة من السيلينيوم تظهر تحولات هيكلية من الأطوار غير المتبلورة إلى الأطوار متعددة البلورات بعد أربعة أسابيع من الترسيب. تفاعلت المرحلة السداسية المتكونة من السيلينيوم بقوة مع $CdBr_2$ السداسية لتشكل خصائص جديدة. من وجهة نظر الهيكل ، يقلل طلاء $CdBr_2$ على Se من كثافة الخلل في Se ، ويزيد من أحجام البلورات ويقلل من نسبة أخطاء التراص. بصريًا ، يتم تشكيل ذيول شريط Urbech ، ويتم تعزيز امتصاص الناقل الحر ، وتقلص فجوة نطاق الطاقة في السيلينيوم. يكون تكوين واجهات $Se/CdBr_2$ مصحوبًا بإزاحة نطاق التوصيل والتكافؤ 1.25 فولت و 0.63 فولت على التوالي. من ناحية أخرى ، أظهرت تحليلات التشتت العازل أن تكوين $Se/CdBr_2$ ينتج عنه أطياف عازلة رنانة. أظهر الجزء الحقيقي من أطياف العزل الكهربائي لـ Se و $CdBr_2$ و $Se/CdBr_2$ التكوين المحتمل لاثنين من مرنان العازل الكهربائي المتمركزين في نطاقات الضوء المرئية والقريبة من الأشعة تحت الحمراء. تضمنت الدراسة هنا أيضًا تحسين معلمات التوصيل البصري للمستقبلات البصرية $Se/CdBr_2$. وقد لوحظ أن الواجهات تُظهر تنقلا أكثر كفاءة عبر الانجراف مع تردد Plasmon الذي يناسب تقنية اتصالات 4G/5G. نعتقد أن الواجهات الضوئية يمكن أن تعمل بشكل جيد في تكنولوجيا الاتصالات الضوئية.